TU/e EINDHOVEN UNIVERSITY OF TECHNOLOGY

A quasi-2D integrated experimental–numerical approach to high-fidelity mechanical analysis of metallic microstructures

Citation for published version (APA):
Vermeij, T., Wijnen, J., Peerlings, R. H. J., Geers, M. G. D., & Hoefnagels, J. P. M. (2024). A quasi-2D integrated experimental–numerical approach to high-fidelity mechanical analysis of metallic microstructures. *Acta Materialia*, *264*, Article 119551. https://doi.org/10.1016/j.actamat.2023.119551

Document license:
CC BY

DOI:
10.1016/j.actamat.2023.119551

Document status and date:
Published: 01/01/2024

Document Version:
Publisher's PDF, also known as Version of Record (includes final page, issue and volume numbers)

Please check the document version of this publication:

• A submitted manuscript is the version of the article upon submission and before peer-review. There can be important differences between the submitted version and the official published version of record. People interested in the research are advised to contact the author for the final version of the publication, or visit the DOI to the publisher's website.
• The final author version and the galley proof are versions of the publication after peer review.
• The final published version features the final layout of the paper including the volume, issue and page numbers.

Link to publication

General rights
Copyright and moral rights for the publications made accessible in the public portal are retained by the authors and/or other copyright owners and it is a condition of accessing publications that users recognise and abide by the legal requirements associated with these rights.

• Users may download and print one copy of any publication from the public portal for the purpose of private study or research.
• You may not further distribute the material or use it for any profit-making activity or commercial gain
• You may freely distribute the URL identifying the publication in the public portal.

If the publication is distributed under the terms of Article 25fa of the Dutch Copyright Act, indicated by the "Taverne" license above, please follow below link for the End User Agreement:

www.tue.nl/taverne

Take down policy
If you believe that this document breaches copyright please contact us at:

openaccess@tue.nl

providing details and we will investigate your claim.

Download date: 08. Feb. 2024

Acta Materialia 264 (2024) 119551

Contents lists available at ScienceDirect

Acta Materialia

journal homepage: www.elsevier.com/locate/actamat

Full length article

A quasi-2D integrated experimental–numerical approach to high-fidelity mechanical analysis of metallic microstructures

T. Vermeij, J. Wijnen, R.H.J. Peerlings, M.G.D. Geers, J.P.M. Hoefnagels *

Department of Mechanical Engineering, Eindhoven University of Technology, 5600MB Eindhoven, The Netherlands

ARTICLE INFO

Keywords:
Integrated testing
Experimental–numerical testing
Crystalline materials
Micromechanics
Crystal plasticity
SEM-DIC
EBSD
2D testing

ABSTRACT

Integrated experimental–numerical testing on bulk metal alloys with fine, complex microstructures is known to be highly challenging, since measurements are restricted to the sample surface, thereby failing to capture the effects of the 3D subsurface microstructure. Consequently, a quantitative comparison of deformation fields between experiments and simulations is hardly possible. To overcome this, we propose a novel 'quasi-2D' integrated experimental–numerical testing methodology that hinges on the fabrication of μm-thin specimens with practically through-thickness microstructures over large regions of >100 μm. The specimens are fully characterized from both surfaces and tested in-situ to retrieve microstructure-resolved deformation fields. Simultaneously, the full microstructure is discretized in 3D and simulated. This allows for a detailed, one-to-one quantitative comparison of deformation fields between experiments and simulations, with negligible uncertainty in the subsurface microstructure. Consequently, a degree of agreement between experiments and simulations is attained which we believe to be unprecedented at this scale. We demonstrate the capabilities of the framework on polycrystalline ferritic steel and dual-phase ferritic–martensitic steel specimens. At the mesoscale, the methodology enables quantitative comparisons of the interaction between multiple grains, while, at the microscale, it enables advancement of numerical models by direct confrontation with detailed experimental observations. Specifically, it is revealed that the individual slip system activity maps, identified with SSLIP, near a grain boundary can only be reasonably predicted by enhancing the adopted crystal plasticity simulations with a discrete slip plane model. Additionally, the experimentally observed strong anisotropic plasticity of martensite can only be captured with a substructure-enriched crystal plasticity model.

1. Introduction

Materials are continuously advanced to achieve improved mechanical properties under challenging conditions. For metal alloys, examples range from single- and multi-phase steels, all the way to complex combinations of large fractions of many elements, such as High-Entropy Alloys (HEAs). In single-phase steels, the competition between various deformation mechanisms, such as Twinning Induced Plasticity (TWIP) or Transformation Induced Plasticity (TRIP), can induce favorable hardening mechanisms [1]. In multi-phase alloys, such as Dual-Phase (DP) steels [2], duplex steels [3], and $\alpha+\beta$-Ti alloys [4], the combination of and interaction between multiple phases, such as strong martensite and soft ferrite [2], yields microstructures that are both ductile and strong. More recent efforts have resulted in the development of HEAs, in which a high mixing entropy between several elements is employed to achieve stable single-phase or dual-phase microstructures which, as the result of the synergistic activation of multiple deformation mechanisms, outperform conventional microstructures [5,6].

With the continuous development of new models that aim to replicate complex deformation mechanisms in these advanced alloys [7–11], experimental validation and calibration become increasingly important. Since the interplay and competition between microscale deformation mechanisms such as twinning, phase transformation and crystallographic slip cannot be calibrated solely by macroscale comparison of experiments and simulations, e.g. through comparison of stress–strain curves, identification efforts must focus at the scale of the microstructure. Currently, however, such studies are either performed on polycrystalline samples, by characterization of the microstructure coupled with the deformation field measured on the sample surface [12–20], or on mono- or bi-crystal specimens, for which the microstructure and deformation can be characterized in full [21–29]. Both approaches have advantages and disadvantages that are outlined in what follows.

To start with the latter, micro- and nanoscale testing is performed through the fabrication of isolated specimens that contain particular micrometer-sized features, such as single crystals or bi-crystals, and are

* Corresponding author.
E-mail address: j.p.m.hoefnagels@tue.nl (J.P.M. Hoefnagels).

https://doi.org/10.1016/j.actamat.2023.119551
Received 13 July 2023; Received in revised form 1 November 2023; Accepted 24 November 2023
Available online 25 November 2023
1359-6454/© 2023 The Authors. Published by Elsevier Ltd on behalf of Acta Materialia Inc. This is an open access article under the CC BY license (http://creativecommons.org/licenses/by/4.0/).

subsequently subjected to micro-bending, micro-pillar compression or micro/nano-tensile testing [21,29–31]. Detailed pre-deformation characterization, well-defined loading conditions and careful *in-situ* multi-microscopy testing allow to observe individual deformation mechanisms in 3D, facilitating quantitative comparisons to simulations [22–28]. However, limitations of specimen fabrication and insufficient spatial resolution of strain measurements restrict applications to specimens with limited microstructural complexity, such as single phases, single grains, and bi-crystals, with some exceptions of (simplified) multi-phase case studies [26,29]. While highly applicable for the investigation of fundamental deformation mechanisms, a concern of most micro- and nanoscale tests is their limited microstructural complexity and the absence of surrounding bulk material, which affects, and may limit, the interplay between distinct deformation mechanisms, while also mostly prohibiting the formation and propagation of damage.

Alternatively, to capture a relevant level of microstructural complexity, an experimental-numerical approach comparing the deformation of bulk samples has been pursued. Experimentally, this involves microstructure characterization of a (small) region on the surface of the sample and deformation mapping through, e.g., *in-situ* Scanning Electron Microscopy based Digital Image Correlation (SEM-DIC). Subsequently, the measured strain fields can be compared to those of simulations, in which a 2D model is usually constructed, assuming a uniform microstructure in out-of-plane direction. The bulk character of the samples induces complex deformation mechanisms, such as propagation of localization bands through the microstructure, strain partitioning between different phases and initiation and propagation of damage [12,13,20]. However, a notorious problem is that only the surface of the sample is accessible for characterization of the microstructure and for *in-situ* deformation measurements. The unknown 3D subsurface microstructure, which can deviate significantly from the assumed extruded surface microstructure, can introduce a significant mismatch between experimental and numerical results, inhibiting proper model validation [12,15]. The numerical study of Zheghadi et al. [32] showed that the subsurface grain morphology has an effect on the free surface, up to a thickness of at least twice the average grain size in single-phase polycrystals. Moreover, variations in the amount of local plastic slip of more than 60% are frequently observed between different subsurface realizations with the same free surface morphology [32]. In DP steel microstructures, subsurface effects up to a thickness of three times the average grain size have been reported [33]. Therefore, detailed knowledge of the subsurface 3D microstructure of the experiment is required to accurately simulate it.

For most engineering alloys, the only conceivable method for 3D characterization is through serial sectioning combined with Electron Backscatter Diffraction, termed as 3D-EBSD [34]. Unfortunately, this is a destructive method and thereby prevents acquisition of the 3D undeformed microstructure in combination with (subsequent) deformation mapping. Shi et al. [18,35] proposed to perform 3D-EBSD on the deformed microstructure with the idea of 'backtracking' the undeformed microstructure using an elaborate optimization scheme. Yet, they only demonstrated this idea on a virtual experiment. An alternative solution is to use a microstructure that is coarse enough to extract specimens with through-thickness, columnar grains, for which the 3D microstructure can be readily estimated and modeled [36]. However, this approach is not applicable to most engineering alloys, since their microstructural features are usually sized in the order of micrometers or smaller, which is especially true for some of the most relevant phases, such as martensite, bainite and pearlite, due to their complex internal substructure. Moreover, even for coarse-grained microstructures, many mechanisms inherently occur at a (sub-)micrometer length scale, such as the interactions of dislocations with grain boundaries and second phase particles.

While these two experimental-numerical approaches have their particular strengths, they involve two distinct configurations. Microscale deformation specimens are well-defined and can be characterized and simulated in detail, containing only 1 or 2 grains, yet lack the occurrence of complex deformation interactions. In contrast, bulk experiments can show advanced micromechanical deformation mechanisms such as strain partitioning and damage, but can hardly be compared quantitatively to (3D) simulations. Therefore, to achieve quantitative experimental-numerical comparisons, in order to unravel advanced deformation mechanisms, an approach is required that can bridge the gap between micrometer-sized and bulk specimens, allowing sufficient complexity on relevant alloys, while retaining full 3D insights.

Therefore, in this work, we propose a new class of experiments based on specimens which are sufficiently thin for their microstructures to be practically uniform in thickness direction, even in the presence of fine-grained microstructural features. This necessitates a thickness in the (sub-)micrometer range, on an area of diameter > 100 μm to capture sufficient microstructural variation, which is achieved through twin-jet electropolishing. The front and rear surfaces of the sample are fully characterized using EBSD and the specimen thickness profile is measured. Subsequently, a pattern is applied which enables strain mapping by DIC [37], accomplished by testing the specimen *in-situ* in an SEM. The resulting microstructural and deformation data is carefully aligned [29] between the two surfaces, resulting in a comprehensive, spatially and time-resolved data set, from which the plasticity mechanisms can be further unraveled through application of a novel slip system identification routine [38].

The through-thickness microstructural uniformity of the proposed ultra-thin specimens allows us to model their full 3D geometry. Each individual grain is discretized by finite elements and advanced crystal plasticity models, taking the crystallographic orientation of all grains and phases into account to model their mechanical response. To ensure the same loading condition between experiment and simulation, the experimentally measured displacements along the edges of the region of interest are employed as boundary conditions in the simulations.

This integrated approach enables a direct comparison of local deformation and plasticity fields, and their evolution, between experiments and simulations of almost the exact same ultra-thin 3D, i.e. 'quasi-2D', microstructure. This, combined with the relatively large through-thickness microstructure area of the specimens, which allows the manifestation of complex deformations, provides an unprecedented platform for validation and calibration of advanced material models, especially those that explicitly take into account the relevant micro-deformation mechanisms, such as (dislocation density) strain gradient plasticity [39], phase transformation kinetics [40] and damage initiation and/or propagation [41].

This paper starts by outlining the dedicated 'quasi-2D' Integrated Experimental–Numerical Methodology in Section 2, using a polycrystalline ferritic specimen. This example demonstrates the high degree of agreement that can be achieved by using a conventional crystal plasticity model on a scale of hundreds of micrometers. Emphasis will be on the capability of performing a quantitative comparison that provides opportunities for a critical assessment of numerical models. The remainder of the paper presents two case studies which highlight critical mechanisms which could be identified by the methodology. In Case Study I (Section 3) we consider a smaller region on the same ferritic specimen, in which a recently-proposed discrete slip plane model, incorporating the stochastics and physics of dislocation sources, is employed to match the discrete slip activity measured experimentally in the vicinity of a grain boundary. Case Study II (Section 4) focuses on a DP steel specimen, with a highly heterogeneous microstructure consisting of soft ferrite and rather hard martensite, in which an enriched crystal plasticity model for martensite is required to match the experimental deformations. Finally, Section 5 gives a brief summary of our conclusions.

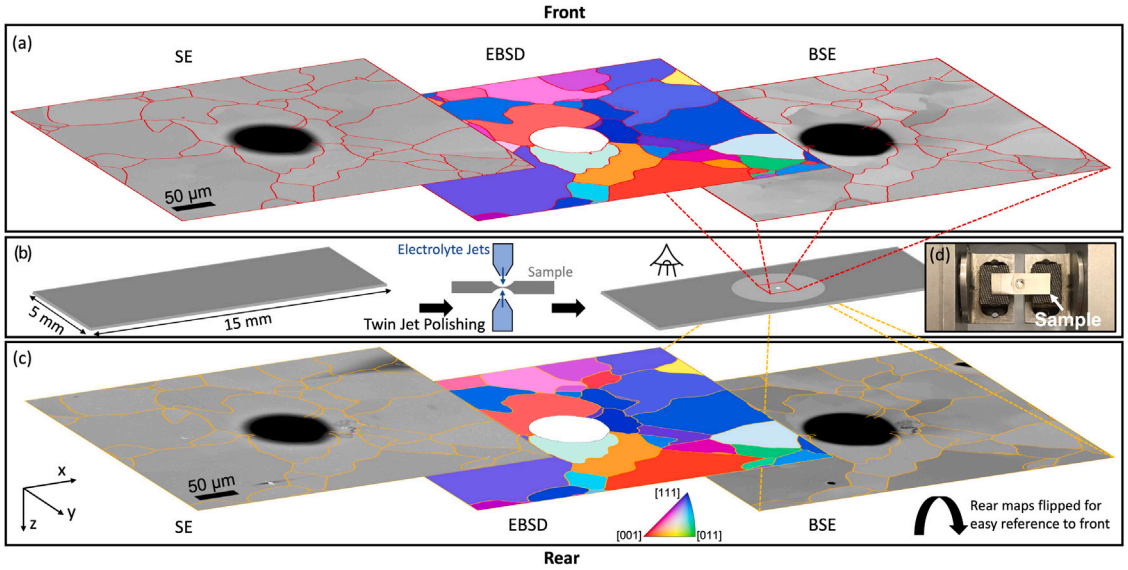

Fig. 1. Overview of sample fabrication and characterization. (a) IL-SE, EBSD and BSE scans of the front surface, with aligned EBSD grain boundaries as overlay in red. (b) Schematic overview of sample fabrication, starting from a rectangular plate in which, through twin-jet electropolishing, a small hole is formed with thin surroundings (not to scale). (c) IL-SE, EBSD and BSE scans of the rear surface, with aligned EBSD grain boundaries as overlay in orange. The rear scans have been flipped to match the front view. (d) Photo of a specimen on the (bottom part of the) clamps of an *in-situ* SEM tensile stage. (For interpretation of the references to color in this figure legend, the reader is referred to the web version of this article.)

2. Integrated experimental–numerical methodology

The 'quasi-2D' methodology will be explained and demonstrated here using an interstitial-free ferritic steel (C0.002-Si0.003-Ti0.03-Nb0.008-Al0.015-Mn0.09 wt%, N28 ppm), which was previously heat-treated to study the fundamentals of slip system activations through micro-tensile testing on single crystal specimens [23], without considering cross-grain interactions. Conventional Crystal Plasticity (CP) will serve as a modeling framework, allowing to demonstrate how numerical simulations can be derived directly from experiments, with subsequent comparison.

2.1. Sample preparation & characterization

An essential part of the methodology is the fabrication of specimens that are thin enough to obtain a through-thickness microstructure over a relatively large area, i.e. $>100 \times 100\ \mu m^2$. To achieve this, we adopt twin-jet electropolishing, which is routinely employed for the fabrication of transmission electron microscopy specimens. It produces a hole in the sample of which the edge is electron-transparent (i.e. having a thickness of less than 100 nm), with increasing thickness away from the hole [42]. First, a sample is cut from a 1 mm thick sheet into a rectangle with size $\sim 15 \times 5$ mm and mechanically ground down to a $\sim 100\ \mu m$ thickness with a 4000 grit finish. This sample size is rather arbitrary; it should be long enough to fit into a tensile stage, small enough to fit into the twin-jet electropolishing machine, and thin enough to yield a high-quality surface after twin-jet electropolishing. Next, twin-jet electropolishing is applied at the center of the sample until a hole is detected with an optical sensor. A Struers TenuPol-5 with Struers A2 electrolyte, which is cooled to ~6°C, employing a flow-rate of 15 at 27.5 V, yields an optimal surface finish for our steels. For the steels in this study, these parameters were determined by using the "scanning function" of the twin-jet polisher and by trial and error. The sample dimensions and the twin-jet electropolishing are shown schematically in Fig. 1(b). A photo of a specimen on top of the clamps of an *in-situ* tensile stage, which will be used to apply deformation, is shown in Fig. 1(d).

Around the hole, the electropolished surface of the front and rear of the sample needs to be of sufficient quality to enable Electron Backscatter Diffraction (EBSD) characterization. On the current sample, SEM scans (using both In-Lens Secondary Electron (IL-SE) and Backscattered Electron (BSE) detectors on a Tescan Mira 3) and EBSD scans (using an Edax Digiview 2 camera) were acquired at 20 kV around the hole, on the front and the rear side, as shown in Fig. 1(a) and Fig. 1(c), respectively. Note that the rear scans are rotated 180° around the x-axis to achieve a front-to-rear view. The EBSD scans, which typically contain significant spatial distortions, are aligned to the SEM scans using a recently proposed alignment framework [29], which is shown here by superimposing the EBSD grain boundaries on the SEM scans. Note that the hole appears to be larger in the BSE scans than in the EBSD maps, since material close to the hole is too thin to generate a sufficient BSE yield. In this paper, all the experimental analysis, including alignment, EBSD data manipulation, and plotting, is performed using the MTEX toolbox in MATLAB [43,44].

Along with the front and rear microstructure, the thickness profile, which gradually increases away from the hole, needs to be measured accurately in order to reconstruct the full microstructural geometry as needed for the 3D discretization. Here, we employ profilometry to obtain a height profile on the front and the rear, which are combined into a thickness map after alignment. In the present case, confocal optical profilometry using a 100× magnification lens on a Sensofar S Neox (using stitching of several height maps) was adopted, yielding the front and rear height maps shown in 3D in Fig. 2(a) and (b), respectively. Fig. 2(c) and (e) show the height maps close to the hole, on front and rear, respectively. A small band is defined around the hole, at a distance of 2 μm from the edge, with a width of 3 μm, as indicated by the black lines in Fig. 2(c) and (e). The data within this band, as defined on the front and the rear, is used for alignment of the two height maps. Here, it is assumed that the material at the hole edge is thin enough (<100 nm) to overlap the surface profiles on the front and rear. Alignment is performed by minimizing the difference in height data in the small band, between front and rear, through 3D rigid body translation and rotation of the rear height map. Subsequently, the full front height map and corrected rear height map are added, resulting in a thickness map, as shown for the small area in Fig. 2(d). Near the hole edge, the thickness fluctuates around zero and at some positions reaches slightly negative values, while gradually increasing away from the hole edge. The negative thickness likely originates from the fact that the sample area within the band is not actually zero thickness

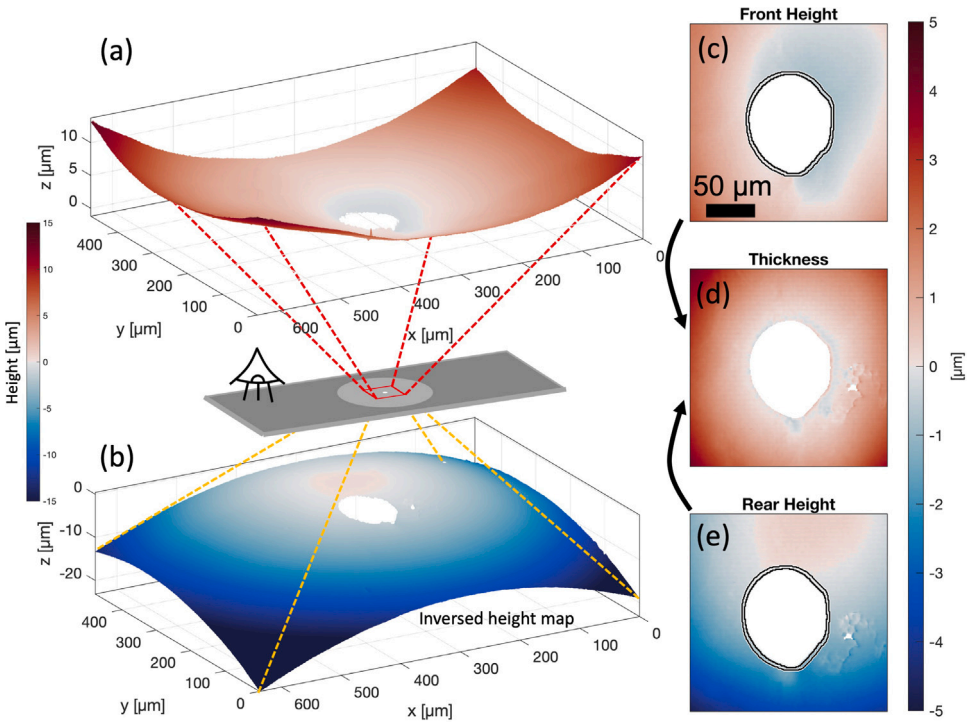

Fig. 2. Overview of the measurement of the specimen thickness map. (a) Front and (b) rear 3D view of the height maps of a $\sim 500 \times 500$ µm^2 area around the hole. The rear height map has been flipped to match the front height map. (c) Front and (e) rear height maps close to the hole edge, with the black lines indicating the small band near the hole edge which is used to align the two maps. (d) Thickness map obtained by adding the front height map and aligned rear height map near the hole edge. (For interpretation of the references to color in this figure legend, the reader is referred to the web version of this article.)

(as assumed), while the thickness can also vary within the band used for the alignment. If the near-hole thickness data is important for the construction of the 3D geometry and mesh, filtering and smoothening can be applied to reduce these fluctuations. Away from the hole the thickness gradually increases to 3–4 µm at a distance of 100 µm.

Before the thickness map and the front and rear microstructure measurements can be combined into a 3D geometry and mesh, all these maps need to be aligned. Similarly to the alignment performed on the height maps to obtain the thickness map, we use the hole edge to align the microstructure and thickness maps. We employ the SEM maps, to which the EBSD data was already aligned (see Section 2.1), and which contain only minor spatial distortions. On all 3 maps (SEM front, SEM rear & thickness) we select 4 homologous points on the hole edge, which are subsequently used to determine the rigid body translation and in-plane rotation to be applied to the SEM rear image and the thickness map to, align them with the SEM front image. Subsequently, both SEM rear (and the earlier aligned EBSD rear data) and the thickness are rotated and translated towards the SEM front configuration, by interpolation to a single regular grid. The aligned experimental data is shown in Fig. 3. While the front and rear EBSD data in Fig. 3(a) and (c) correspond to those in Fig. 1, the thickness map in Fig. 3(b) also shows the front and rear EBSD grain boundaries as an overlay, using red and orange lines respectively. Notably, these boundaries overlap almost perfectly near the hole, where the sample is the thinnest and one therefore expects the front and rear surface scans to match the best. This indicates that the rear-to-front alignment was successful. At a larger distance from the hole, a more substantial mismatch between the front and rear grain boundaries is observed — to a maximum of approximately the local thickness of the sample. In these region we also observe slight differences in topology between front and rear surface. Both of these observations imply that the assumption of a uniform through thickness microstructure no longer holds. Within a distance of approximately 100 µm it however is quite accurate.

2.2. 3D geometry extraction and discretization

In order to construct a 3D Finite Element (FE) discretization that is suitable for simulations, we need to establish a 3D geometry of the grains measured on the front and rear surface. For this we consider the front and rear grain data and the thickness profile, within the black rectangle in Fig. 3(a, b, c) and process it as follows.

The 3D geometry is reconstructed based on a separate level-set function for the front and rear surface of each grain. Each level-set is a function of two independent variables, i.e. the in-plane spatial coordinates x and y, of which the zero contour corresponds to the outer edge of the grain in the respective surface of the specimen [45]. Here, signed-distance functions (SDFs) are used, which are special types of level-set functions in which the absolute value of the function at a point is equal to the shortest distance of that point to the zero iso contour, while the value is negative in the interior of the geometry and positive in the exterior. One advantage of using this implicit geometry description is that the geometry can be easily modified by manipulating its level-set functions.

A method similar to warp-guided distance field interpolation [46, 47] is used to reconstruct the 3D grain morphology. The position vector $\vec{x} \in \mathbb{R}^3$ is decomposed into an in-plane vector $\vec{x}_2 \in \mathbb{R}^2$ and an out-of-plane component z. The 2D SDFs of grain i on the front and rear surfaces are denoted $DS_i^{\mathrm{F}}(\vec{x}_2)$ and $DS_i^{\mathrm{R}}(\vec{x}_2)$, respectively. The through thickness grain morphology is obtained by linear interpolation of the surface SDFs, given by the 3D SDF

$$\phi_i(\vec{x}) = \alpha^{\mathrm{F}}(\vec{x})\, DS_i^{\mathrm{F}}\left(W_i^{\mathrm{F}}(\vec{x})\right) + \alpha^{\mathrm{R}}(\vec{x})\, DS_i^{\mathrm{R}}\left(W_i^{\mathrm{R}}(\vec{x})\right), \tag{1}$$

with interpolation coefficients

$$\alpha^{\mathrm{F}}(\vec{x}) = \frac{z - h^{\mathrm{R}}(\vec{x}_2)}{h^{\mathrm{F}}(\vec{x}_2) - h^{\mathrm{R}}(\vec{x}_2)} \tag{2}$$

and

$$\alpha^{\mathrm{R}}(\vec{x}) = \frac{h^{\mathrm{F}}(\vec{x}_2) - z}{h^{\mathrm{F}}(\vec{x}_2) - h^{\mathrm{R}}(\vec{x}_2)}, \tag{3}$$

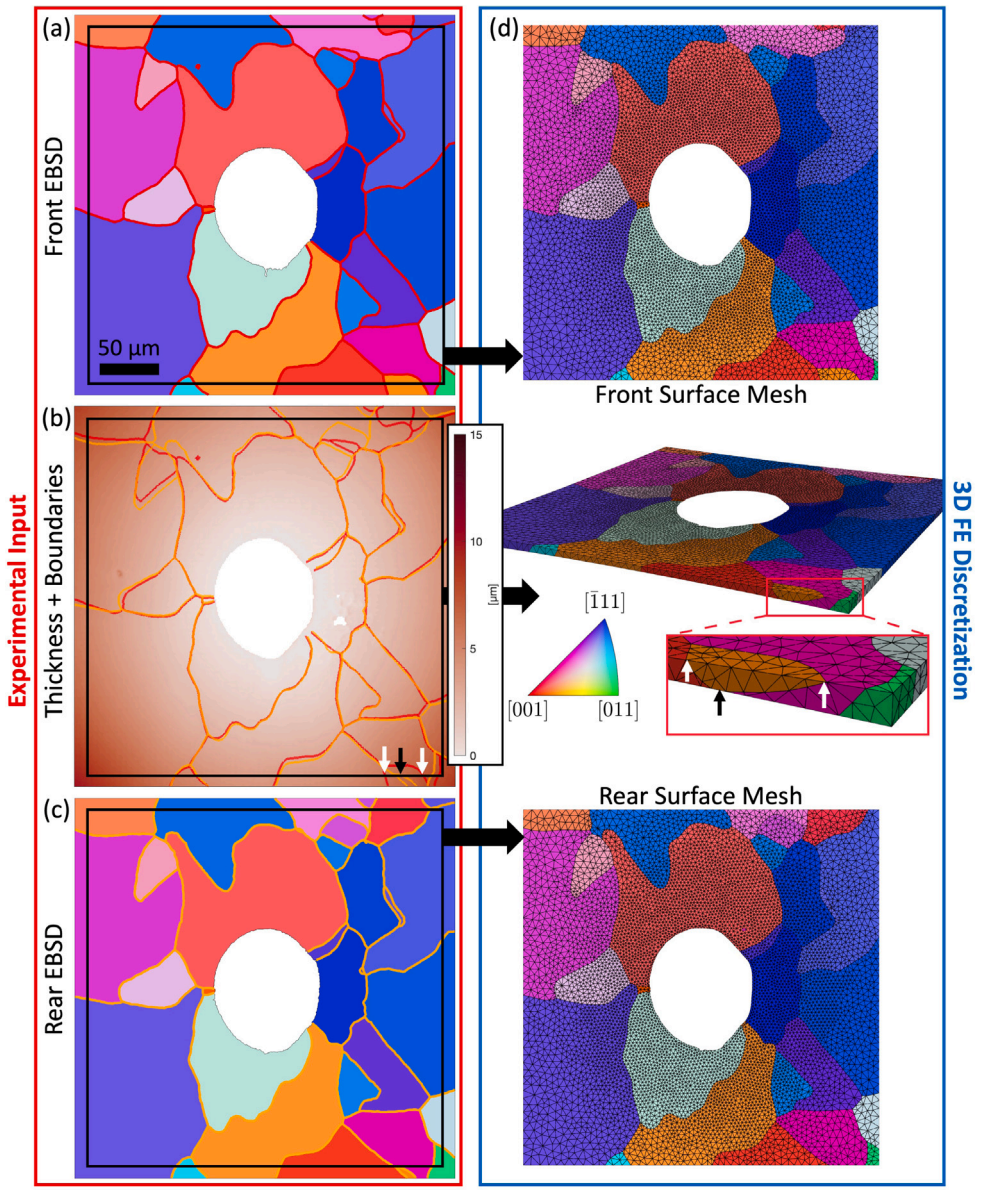

Fig. 3. Overview of the creation of a 3D FE mesh from the experimental characterization data. (a) EBSD map of the front of the specimen. (b) Thickness map with overlay of front and rear EBSD grain boundaries, in red and orange respectively, showing the result of the alignment between rear microstructure, thickness map and front microstructure. (c) EBSD map of the rear of the specimen. In (a, b, c) the black square shows the area which is modeled. (d) The constructed 3D mesh, shown from multiple angles (front, 3D and rear), with a zoom of the 3D mesh highlighting how boundaries can also vary over the thickness. The arrows in (b) and (d) highlight how strong variations in grain shape between front and rear are accurately captured in the mesh, with the white arrows indicating features on the front side (red grain boundaries in (b)) and the black arrow indicating the small footprint of the same grain on the rear surface (orange grain boundaries in (b)). (For interpretation of the references to color in this figure legend, the reader is referred to the web version of this article.)

where $h^{\mathrm{F}}(\vec{x}_2)$ and $h^{\mathrm{R}}(\vec{x}_2)$ are the height profiles of the front and rear surfaces, respectively. In this work it is assumed that the thickness profile is symmetric, such that $h^{\mathrm{F}}(\vec{x}_2) = -h^{\mathrm{R}}(\vec{x}_2)$ and $h^{\mathrm{F}}(\vec{x}_2)$ is half the thickness profile shown in Fig. 3(b). Furthermore, warp functions are introduced, given by

$$W_i^{\mathrm{F}}(\vec{x}) = \vec{x}_2 + \alpha^{\mathrm{R}}(\vec{x}) \left[\vec{c}_i^{\,\mathrm{R}} - \vec{c}_i^{\,\mathrm{F}}\right] \tag{4}$$

and

$$W_i^{\mathrm{R}}(\vec{x}) = \vec{x}_2 + \alpha^{\mathrm{F}}(\vec{x}) \left[\vec{c}_i^{\,\mathrm{F}} - \vec{c}_i^{\,\mathrm{R}}\right], \tag{5}$$

where $\vec{c}_i^{\,\mathrm{F}} \in \mathbb{R}^2$ and $\vec{c}_i^{\,\mathrm{R}} \in \mathbb{R}^2$ are the centroids of the grain on the front and rear surface, respectively. Their use in Eq. (1) implies that the interpolation is done in the direction of the line connecting the two centroids (through the thickness) [46,47].

The 3D morphology of each grain observed on the front and rear surface is reconstructed by Eq. (1). The zero contour of this function represents the grain boundaries through the thickness. However, this method does not guarantee that the boundaries of the grains are fully connected, i.e., empty spaces may remain e.g. at triple junctions, while grains may overlap elsewhere. To remedy this problem, a generalized Voronoi-like approach is used to calculate the final implicit 3D descriptions of the grains [48]:

$$O_i(\vec{x}_2, z) = \phi_i(\vec{x}_2, z) - \min_{j \neq i} \phi_j(\vec{x}_2, z). \tag{6}$$

This equation effectively grows or shrinks each grain to the mid-planes between itself and its closest neighboring grains. Note that the result of Eq. (6) is not a SDF anymore. However, it is still a level-set function of which the zero contour defines the surface of a grain. If needed, it can be converted to a SDF by solving the Eikonal equation, e.g. with the fast-marching method [49].

The above-described interpolation procedure cannot be used for grains that are visible only on one surface of the specimen. Such grains, which occasionally occur therefore need a special treatment. They are first extruded to a depth of half the thickness of the specimen, i.e., to the midplane. To this end, Eq. (1) is bypassed and a 3D SDF, $\phi_i(\vec{x})$, corresponding to this half-columnar geometry is directly constructed based on the front/rear 2D SDF. The Voronoi approach of Eq. (6) then grows or shrinks these grains, taking into account the geometry of the surrounding grains.

All the above-defined level set functions are computed on the domain. Due to the through-thickness interpolation and the Voronoi approach, the zero contour of the level set of a grain at the edge of the domain extends outside of the domain. The domain boundaries can be taken into account by clipping the level set functions of individual grains with a SDF describing the shortest distance to the domain boundary, $\phi^{\mathrm{D}}(\vec{x})$, with negative values inside the domain. The clipped level set function of a grain, $O_i^{\mathrm{D}}(\vec{x})$, is given by

$$O_i^{\mathrm{D}}(\vec{x}) = \max\left(O_i(\vec{x}), \phi^{\mathrm{D}}(\vec{x})\right). \tag{7}$$

Note that if both $O_i(\vec{x})$ and $\phi^{\mathrm{D}}(\vec{x})$ are SDFs, then $O_i^{\mathrm{D}}(\vec{x})$ is also a SDF.

The resulting implicit descriptions of all the grains are used as input for the finite element discretization algorithm described by Bastiaansen et al. [50]. This algorithm converts the implicit grain boundary descriptions to a set of surface meshes, which are then used as input for a 3D mesher (Tetgen) to obtain a grain boundary conforming volume mesh. As an example, the final mesh of the geometry, of Fig. 3(a, b, c) is shown in Fig. 3(d), in front view, (flipped) rear view and in 3D view, with a zoom on one of the edges. The mesh consists of 65.032 quadratic tetrahedral elements, which perform well in CPFE simulations [51], and 112.851 nodes. A comparison between the experimental microstructure maps and the resulting 3D discretization reveals that the front and the rear surfaces match practically perfectly. In most of the domain, the grain shapes also match well between front and rear, and most of the through thickness grain boundaries therefore are practically vertical. Close inspection of the 3D view shows how the thickness of the mesh varies strongly between the central hole and the outer edge. On the lateral surfaces, which represent cross sections of the thick of parts of the samples, non-perpendicular grain boundaries occur. Additionally, the zoom of the edge of the 3D mesh reveals how well we can capture strong changes of grain shape between front and rear, which results in tilted boundaries through the thickness. This effect is highlighted by the white and black arrows in Fig. 3(b) and (d), indicating a grain which is large on the front and tiny on the rear.

2.3. Mesoscale and microscale experimental strain mapping

Experimentally, we require the measurement of deformation fields on the specimen, which is done here by performing SEM-DIC. In the considered '2D' tests it can be highly valuable to monitor the deformation of multiple grains in a mesocale Region of Interest (RoI), with a size of $\sim 300 \times 300\ \mu m^2$, while simultaneously focusing on a number of microscale RoIs, of $\sim 40 \times 40\ \mu m^2$, to study specific micro-deformation mechanisms at a higher spatial resolution. Such a multi-scale analysis, however, poses a problem in terms of application of the random DIC speckle pattern, which needs to be suitable for both mesoscale and microscale monitoring, in conjunction with separate SEM imaging conditions and image correlation settings optimized for both scales. It is known from the literature that the ideal speckle size is three times the pixel size [52,53], while a highly dense pattern with full coverage of particles is desired for maximum spatial resolution. Therefore, in theory, optimal DIC quality is achieved using a multi-scale pattern with both larger and smaller speckles/particles [37,54]. Yet, it is hard to achieve a combination of larger speckles, in the order of 75 nm ($\approx$ 300 μm/4096pixels), and smaller speckles, in the order of 10 nm ($\approx$ 40 μm/4096 pixels), as ideally needed for the '2D' tests here. Instead, one could opt to perform single-scale scans of the size of the mesoscale RoI using the microscale pixel size, to combine the mesoscale and microscale analysis in single scans. However, this requires a stable SEM scan generator that can produce very large scans, that will compromise on the size of the field of view and the desired spatial resolution. Therefore, we employ a multi-scale DIC analysis using a single DIC pattern for both the meso- and microscale. The specific details of the optimized DIC patterning and measurement parameters are given next. Note that these may differ if different equipments or tools are used (Sputter coater type, SEM, DIC software, etc.).

An InSn DIC speckle pattern is applied, both on the front and the rear of the specimen, by employing the one-step patterning method introduced by Hoefnagels et al. [37], using an InSn sputter coating process with the following parameters: 9×10^{-3} mTorr chamber pressure, 20 mA current, 1.5 min sputtering time, ~85 mm target-to-sample distance. This results in a high density random pattern with a ~25–60 nm speckle size, which is optimal for microscale DIC specifically. A variety of larger InSn particles also provide sufficient contrast for mesoscale DIC, albeit at a lower quality as compared to the pattern for the microscale DIC analysis.

The deformation is applied *in-situ* using a micro-tensile stage (Kammrath & Weiss) in a Tescan Mira 3 SEM. Since the sample is only very thin at the center, and not at its outer edges, (see the sketch in Fig. 1(b)), it can be easily handled and clamped into a regular *in-situ* tensile stage, see Fig. 1(d). However, this also means that the thin specimen cross-section constitutes less than 1% of the full sample cross-section, rendering the force measurements unusable to generate a stress–strain curve that can be compared to the simulations. For deformation monitoring, we employ in-lens SE imaging at a 5 kV beam voltage and a 5 mm working distance, since this provides optimal conditions to scan the SEM-DIC pattern in our system. At the mesoscale, the region around the hole with a field of view of 350 μm (4096 pixel scans) is tracked, see Fig. 4(a) for the undeformed DIC image, with a zoom in Fig. 4(b_1). Tension in x-direction is applied, with in-lens SE imaging performed at 4 successive stages of global strain levels of $\bar{\varepsilon}_{xx} = 0.006$, 0.010, 0.016 and 0.028. These are defined as a linear strain, based on the measured extension between the left and right side of the hole, in x-direction. The microscale deformations are mapped at the same deformation increments on areas limited to either 30 μm or 40 μm field of view (for scans of width 3072 or 4096 pixels, for a pixel size of ~10 nm). Since the full 350 μm region is too large to be fully resolved at microscale strain resolutions in feasible experimental time frames, a selection of a smaller number of microscale regions is required. For the current sample, we chose 5 areas of interest: 1 inside a grain, 2 at a grain boundary and 2 at a triple junction. Only 3 of these areas (indicated with white dashed rectangles in Fig. 4(a)) revealed significant deformations and are therefore discussed in what follows. The fine DIC pattern for these magnifications is shown in Fig. 4(b_2). At the rear, microscale SEM-DIC scans were acquired, at approximately the same locations, solely before and after testing the specimen, since the rear surface is inaccessible as long as the specimen is clamped in the tensile stage. The rear deformation maps can verify that plasticity occurs through the thickness and can shed light on the 3D deformation kinematics.

In the test used for illustration here, the deformation was applied directly after microstructure characterization. However, for future experimental–numerical analyses using the '2D' specimens, the microscale region of interest selection may be done based on preliminary simulations of a large region, using approximate local boundary conditions (e.g. obtained by running a simulation on a full '2D' specimen with a hole using a simple isotropic plasticity model) before actually testing the specimen.

For the mesoscale SEM-DIC scans, with a relatively low pattern quality, DIC is performed with VIC-2D (Correlated Solutions) because of its high noise robustness, using a relatively large subset size of 61 pixels (5.2 μm), with step size of 1 pixel (85 nm). On the other hand, for the microscale SEM-DIC images, with high pattern quality, DIC

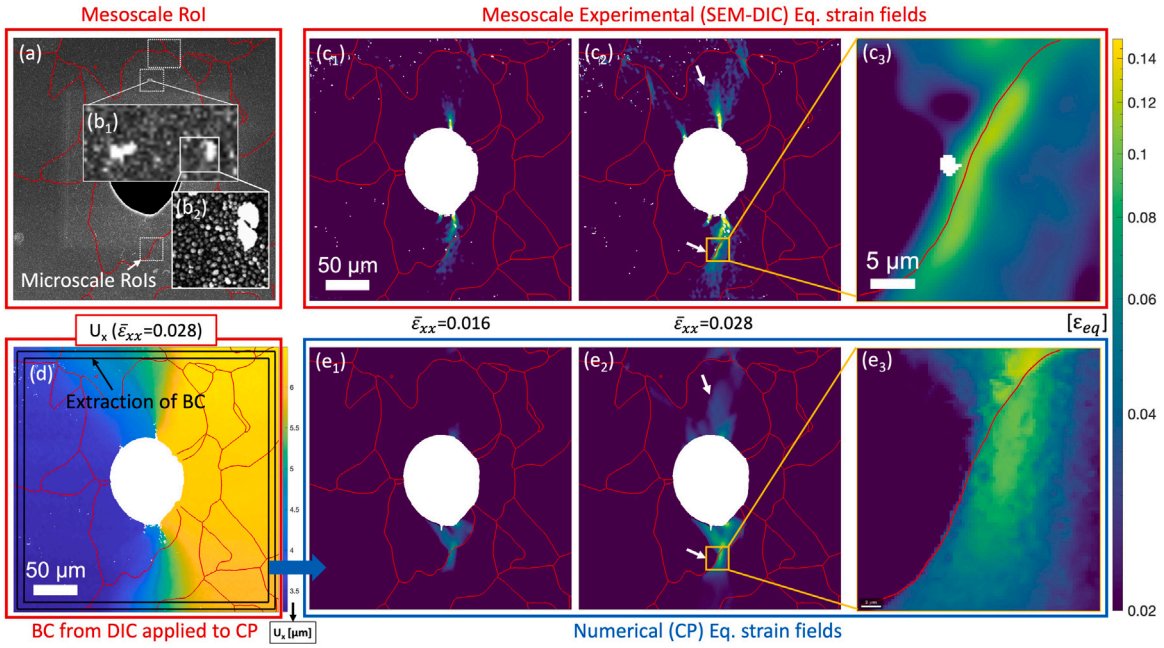

Fig. 4. Frontside mesoscale deformations obtained from experiments and simulations. (a) Mesoscale SEM-DIC reference pattern, with the three white dashed rectangles indicating the regions which are tracked for microscale strain mapping (see Fig. 5). (b_1) zoom-in to illustrate the mesoscale DIC pattern quality, as observed with the mesoscale SEM imaging settings, whereas (b_2) shows a zoom-in of the microscale DIC pattern, which is employed for the measurements of Fig. 5. (c) Mesoscale experimental equivalent strain fields at global strains of $\bar{\varepsilon}_{xx} = 0.016$ and 0.028, for (c_1) and (c_2), respectively, with (c_3) showing a zoom of the region around the grain boundary. (d) The x-component of the experimental mesoscale displacement field at 0.028 global strain. The area between the black contours is averaged into a line profile through Gaussian filtering (spanning the full perimeter of the mesoscale RoI) and employed as boundary conditions to the 3D model. (e) Mesoscale numerical 2D equivalent strain fields at the same global strain levels, in (e_1) and (e_2), with the same zoom in (e_3). The simulated strain maps have the same color scale as the experimental ones. The white arrows in (c_2) and (e_2) indicate notable areas of adequate experimental–numerical agreement. In all subfigures, (frontside) EBSD grain boundaries are drawn as red lines. Tension is applied horizontally. (For interpretation of the references to color in this figure legend, the reader is referred to the web version of this article.)

is performed with MatchID to achieve the best compromise between spatial resolution and accuracy of the strain maps [20,29], using in this case a small subset size of 21 pixels (210 nm), with a step size of 1 pixel (10 nm). In both cases, filtering of the displacement maps, strain calculation and microstructure-to-strain alignments were performed as described in detail by Vermeij et al. [29,55]. In previous work, we have measured the strain resolution, based on steps in strain in a pearlite lamellar structure, where the strain was computed in the same way and based also on DIC on ~3 pixel sized speckles. This yielded a strain resolution that is ~0.15 times the subset size [55]. Applying this to the current situation yields an estimate of the strain resolution of 750 nm and 30 nm for the large and small RoI, respectively. In the current paper, unless specified otherwise, 'equivalent strain' refers to a 2D von Mises strain, calculated from the Green Lagrange strain tensor, which is defined and motivated in Refs. [29,55].

Next, we will showcase the richness of the data generated by the integrated framework; a more detailed discussion of the results will follow in Case Study I in Section 3. Fig. 4(c_1, c_2) shows the mesoscale 2D equivalent strain fields at global strain levels of $\bar{\varepsilon}_{xx} = 0.016$ and 0.028, with superimposed EBSD grain boundaries, after alignment [29]. It can be observed that, for increasing levels of global strain, deformations predominantly occur above and below the hole, which is expected due to the inherent stress concentration introduced by the hole. We also show the x-component of the displacement field at the final load increment in Fig. 4(d), which demonstrates how the specimen deforms globally. The two components of the displacement field in a region along the boundary of the RoI will be used to extract the boundary conditions for the numerical simulations.

The microscale strain fields are shown in Fig. 5 for the RoI with a single grain in (a), the grain boundary in (b) and the triple junction in (c). For each small region, e.g. for the single grain in (a), three out of the four acquired front-side microscale strain maps are shown in (a_1), (a_2) and (a_3), and the (single) rear-side microscale strain map in (a_4). The same subfigure structure is employed for the grain boundary and the triple junction, in Fig. 5(b) and (c), respectively. All plots have EBSD-derived grain boundaries as overlay, drawn in red and orange, for the front and rear respectively.

2.4. Quantification of plasticity by SSLIP

Assessing the experimental microscale strain fields in Fig. 5, it is obvious that these fields reveal discrete strain distributions, as is expected at this scale for crystallographic slip. In the single grain region (Fig. 5(a)), slip traces are predominantly visible at the bottom of the area, which is near the hole, where the material is thinner. The slip traces fade out towards the top of the region, where the material is thicker. In the region with the triple junction (Fig. 5(c)), slip activity is primarily observed in the grain to the right of the triple junction. Slip transfer takes place between the bottom and top-right grain, while the top-left grain appears to impede plastic deformation. The grain boundary area (Fig. 5(b)) will be subjected to a more detailed investigation in case study I (Section 3.2).

While the equivalent strain fields in Fig. 5 can be employed for the assessment of the local deformations, proper investigation of anisotropic plasticity, such as crystallographic slip or deformation twinning, requires more advanced analysis routines. Therefore, another important aspect of the integrated methodology is the quantification of specific plasticity mechanisms, in the form of crystallographic slip systems in the current work. While the slip magnitude of every individual slip system can easily be retrieved from crystal plasticity simulations, since it is computed in every integration point, this is not trivial in experiments. A standard slip system identification routine involves identification of slip lines in the strain fields and to match these to theoretical slip traces, yet this ignores the slip direction [56]. More accurate identification methods have been developed based on the displacement jump across the slip trace [57,58], requiring straight

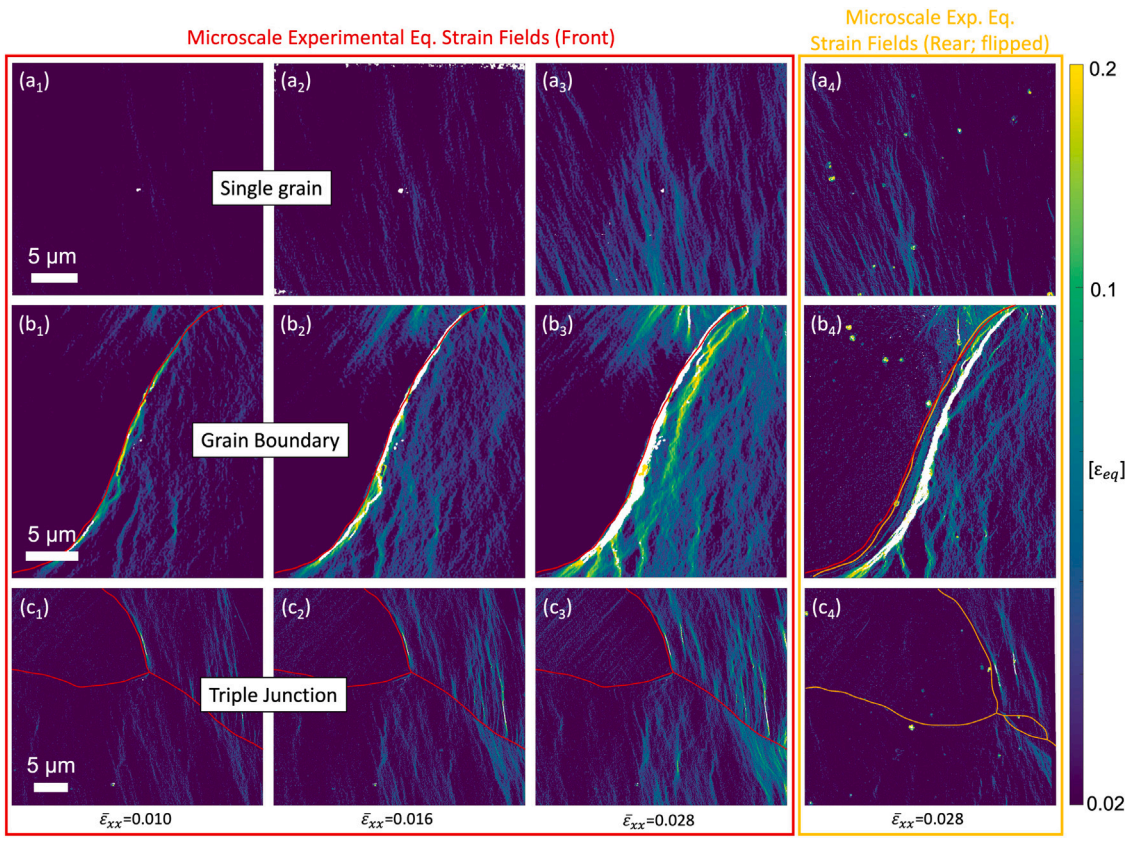

Fig. 5. Deformation fields on three small areas (as indicated Fig. 4(a)) with (a) a single grain, (b) a grain boundary and (c) a triple junction. For each region, e.g. the single grain in (a), microscale strain fields, on the front side, at global strains of $\bar{\varepsilon}_{xx} = 0.010$, 0.016 and 0.028, are plotted in (a_1), (a_2) and (a_3), respectively. (a_4) shows the rear microscale strain fields, acquired after testing. For the grain boundary in (b) and the triple junction in (c), the same subfigure structure is employed. The white datapoints were unsuccessfully correlated by DIC. Front-side EBSD grain boundaries are drawn as red lines and rear-side EBSD grain boundaries are drawn as orange lines. (For interpretation of the references to color in this figure legend, the reader is referred to the web version of this article.)

and/or discrete slip events. However, the slip bands in the strain fields (e.g. Fig. 5(b)) are not at all straight, nor discrete, but instead are curved and wavy, indicating the occurrence of cross slip.

To mitigate these limitations, we employ a recently proposed local slip system identification method, termed SSLIP (for Slip Systems based Local Identification of Plasticity), which is capable of yielding a slip activity field for every considered slip system [38]. The SSLIP method exploits the measured 2D displacement gradient tensor, computed by taking the gradient of the DIC displacement fields, to estimate the most likely combination of active slip systems, each with its own magnitude, for each individual data point in the deformation map [38]. The SSLIP approach will be employed for a quantitative comparison to simulations in case study I, in Section 3.2.

2.5. Material model and boundary conditions

Integral to the quasi-2D methodology is a numerical solution strategy to simulate the mechanics of the full 3D geometry, which includes 3D grains that are constructed from the measured 2D crystallographic orientation maps and thickness profile, see Section 2.2. The integrated method employs the Finite Element Method (FEM) to simulate the mechanics, utilizing the constructed 3D discretization and allowing the use of a large range of material models. Here, however, we will employ Crystal Plasticity (CP), as it suits our material best and serves best to demonstrate the methodology. To mirror the two scales of observation of the experiments, we employ a conventional CP model at the mesoscale (in the current section) and an advanced discrete CP model at the microscale (in case study I in Section 3). Since both models are not integral to the methodology, they are described in more detail in Appendices A.1 and A.2.

Besides the 3D discretization and the material model, also the boundary conditions are pivotal to the integrated quasi-2D testing methodology, as they must accurately reflect the local loading conditions of the RoI of the thin specimens. To this end, the boundary conditions are extracted from the experiment. This is required because uniaxial tension, which is commonly assumed in integrated studies [12,13], is only valid for the sample on a global level, but not necessarily locally. For the considered quasi-2D specimens, this validity is even more questionable, since the specimen's thickness strongly varies around the hole. Moreover, previous studies have shown that the application of experimentally measured boundary conditions is of great benefit, and in some cases required, for a proper integrated experimental–numerical analysis [28,35,59]. Moreover, the application of measured boundary conditions can alleviate the missing experimental stress–strain curve. The measured deformations can potentially act as a local force sensor by assuming knowledge of the (anisotropic) elasticity parameters [59], especially as the thicker specimen area may not deform fully plastically.

Here, we extract the boundary conditions from the displacement fields as measured by SEM-DIC. At the (in-plane) location of the outer boundary of the 3D mesh (see Fig. 4(d)), the (x- and y-) displacement data is extracted, after Gaussian blurring with a standard deviation of ~10 datapoints (~1 μm at the mesoscale), to reduce noise, and is then interpolated towards the boundary nodes of the mesh. Note that the SEM-DIC data only provides 2D (in-plane) displacements. In the out-of-plane direction, all nodes (except 1 to avoid rigid body motion) are free to move, which seems reasonable due to the thin nature of the '2D' specimens. The measured deformation is applied to the numerical model in ~1000 increments (time steps). The displacements applied in these increments are interpolated linearly between the 4 measured displacement increments.

As an example, the resulting frontside 2D equivalent strain fields of a FEM simulation with the conventional CP model are displayed in Fig. 4(e_1) and (e_2), at the same increments at which the experimental equivalent strain fields are plotted. Note that the size of the area, the location of grain boundaries, and the colorscale of the strains, are all identical between the experiments and simulations. The conventional CP appears to be suitable to capture the relevant deformation mechanisms occurring in the mesoscale experimental strain maps, as will be further explored below. In contrast, the microscale areas show discrete plasticity (Fig. 5) and require a discrete plasticity model for simulations.

2.6. One-to-one experimental-numerical comparison

A key feature of the '2D' integrated framework is the ability to perform a direct comparison between experimental and numerical deformation fields. The mesoscale strain fields in Fig. 4 match reasonably well, with deformations occurring predominantly above and below the hole. Moreover, there are several locations (see white arrows in Fig. 4(c_2) and (e_2), and the zooms in (c_3) and (e_3)) where the experimental–numerical agreement is adequate, considering the simplicity of the conventional CP material model used for these FEM simulations. However, several aspects of the deformation field, such as the strain magnitudes and the heterogeneity of the strain distribution, do not match well. Moreover, comparison of the numerical and the microscale experimental equivalent strain fields reveals more discrepancies. The microscale experimental deformations are clearly more heterogeneous, especially on the right side of the grain boundary in Fig. 5(b_{1-4}), compared to the smooth simulation data (Fig. 4(e_3)). Indeed, it is clear that the simulations are missing a considerable number of intricate details, and that more advanced simulations are required.

Next, the one-to-one comparison is employed to critically assess which aspects of the quasi-2D integrated methodology are of importance to enable an accurate comparison of experimental and numerical deformation fields. We demonstrate this here by assessing which methodology ingredients need to be included for the example of polycrystalline ferrite and how they contribute to the experimental-numerical identifiability. While the selected material model of the simulations is not an ingredient of the quasi-2D integrated testing methodology, it is under study in the methodology and is therefore also considered here. We assess the following aspects: (i) the precise shape of the hole, (ii) the adoption of the thickness profile and (iii) the correct use of the crystal orientations. To this end, the mesoscale experimental and (reference) numerical equivalent strain fields are shown again in Fig. 6(a) and (b), respectively, in order to compare them to 4 instances of a simulation in which one of the aspects was investigated. First, Fig. 6(c) shows the simulation with an elliptical hole shape, instead of the one replicated from experiments. Interestingly, little difference can be observed, likely because the material is very thin near the hole edge and therefore does not significantly influence the behavior further away from the hole. Next, the thickness profile is ignored and instead kept constant (at 5 μm), for which the result is plotted in Fig. 6(d). In this case, the strain field is significantly different, predominantly showing deformation in a smaller area close to the hole. Finally, we employ 2 sets of random crystal orientations for the microstructure in Fig. 6(e) and (f), instead of those measured experimentally. In these two strain maps, the positions where deformations occur are considerably different. For instance, strains around the grain boundary below the hole reveal different patterns for both cases of random orientations, contradicting the reference simulation. Hence, the sample thickness profile and the correct crystal orientations are both required to enable an accurate comparison between experiment and simulation. The effect of the crystallographic anisotropy will be further investigated in case study I. Accurately capturing the morphology of the hole is less important.

3. Case study I: discrete microscale ferrite plasticity

The experimental polycrystalline ferrite deformation patterns can be simulated with conventional CP with reasonable accuracy on the mesoscale, as was shown in Fig. 4. However, as discussed in Section 2.6, at the microscale, plasticity is more discrete and requires an alternative modeling approach in which the plasticity mechanisms that are induced by the underlying dislocation network are modeled more realistically. Therefore, in this case study, we assess the numerical–experimental match of a recently developed 'discrete slip plane' framework [10] that introduces sub-grain heterogeneity of plastic slip into the simulations by a stochastic variation of the initial slip resistance which mimics the presence of dislocation sources and obstacles to dislocation glide. An advantage is that its implementation can be done in a standard CP FEM framework, through which we avoid the use of other approaches, such as Discrete Dislocation Dynamics (DDD), that are computationally much more expensive. In this case study, we focus on the region with a single grain boundary, since it shows an interestingly strong interaction with a grain boundary.

Before constructing the model, we re-assess the experimental microscale DIC data, as this will be used to extract boundary conditions for the simulations. However, in this case, only the data at the microscale will be adopted. In Fig. 7(a), a map of the x-component of the displacement field is shown, for the final increment. The white datapoints, which form regions that are enclosed by the magenta contour lines, predominantly to the right of the grain boundary, were not successfully correlated by DIC due to strong strain localizations. To enable the usage of this data for extracting boundary conditions, and to ensure the full experimental deformation field can be compared to the simulations, we perform interpolation of the displacement fields, using cubic shape functions. The equivalent strain field after interpolation is shown in Fig. 7(c) (including a zoom in (b)), wherein the interpolated regions again are marked by magenta contour lines. The left side of the interpolated area corresponds closely to the grain boundary (in red), suggesting that the plasticity occurs solely in the grain to the right of the boundary.

3.1. Discrete slip plane model

The discrete slip plane (DSP) model [10], in which slip resistances vary locally within a single grain, is adopted here. In this model, the slip resistances of each atomic plane and direction are sampled based on a probability density function, which characterizes the likelihood of (i) finding a dislocation source on the plane and (ii) the activation stress of that source, as a function of the dimensions of the grain and specimen. To render the problem numerically tractable, all atomic glide systems in a grain are collected in a number of bands with width l. This is done separately for all slip systems, i.e. bands of different slip systems are crossing each other. It is assumed that if the band width l is sufficiently small, only the weakest atomic plane in a band, i.e. that plane with the lowest initial slip resistance, carries the plastic deformation. This implies that it is the initial slip resistance, and its evolution, of this softest plane which governs the response of the entire band. The FE implementation of the model is based on conventional CP, whereby the value of the initial slip resistance in each FE integration point within the slip system band is set equal to the slip resistance of the weakest atomic plane in that band. Further details on the implementation can be bound in Appendix A.2 and in Wijnen et al. [10].

The probability density function for sampling the slip resistances of each atomic plane is based on the concept of a single-arm dislocation source. For the ferrite phase, the exact distribution and the adopted parameters have been identified from micro-tensile tests of single crystal ferrite specimens (of the same steel grade), and can be found in Wijnen et al. [60]. The adopted band width equals $l = 1$ μm. In Fig. 7(d, e), the initial slip resistance (CRSS) field of the slip system with the highest Schmid factor (see also Figs. 8 and 9) of both grains is depicted

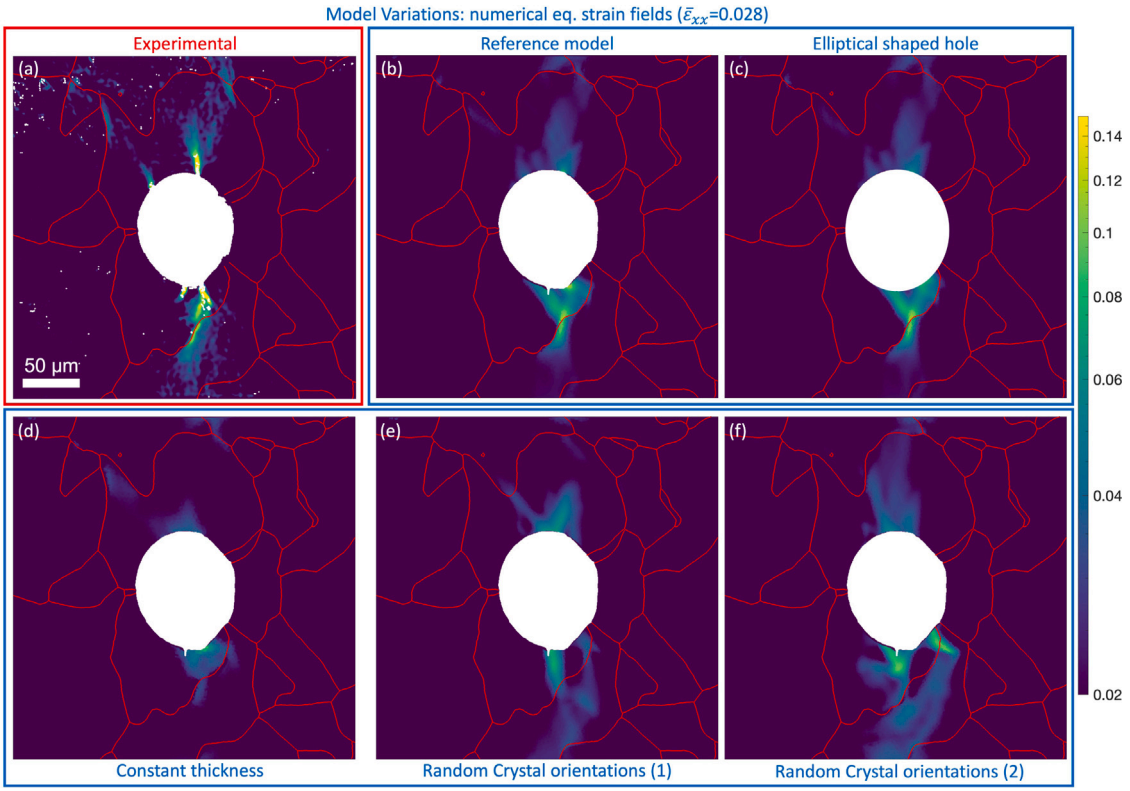

Fig. 6. A study of essential aspects of the 'quasi-2D' integrated testing methodology at $\bar{\varepsilon}_{xx}$ = 0.028. (a) Reference mesoscale experimental equivalent strain field. (b, c, d, e, f) Numerical equivalent strain fields for varying model choices, where in each case only one model choice is varied compared to the 'reference' model shown in (b), for which all model choices have been implemented in the most accurate manner. In (c), the experimentally derived hole shape is changed into an ellipse for the simulation. In (d), the experimentally measured thickness profile is replaced by a constant thickness in the simulation. In (e) and (f), the measured crystal orientations are replaced by random orientations. In all subfigures, front-side EBSD grain boundaries are drawn as red lines. (For interpretation of the references to color in this figure legend, the reader is referred to the web version of this article.)

for two different realizations (with FEM mesh overlay), where each realization is obtained by randomly sampling the (same) probability density function of atomic-plane slip resistances. These plots serve to illustrate (i) how the heterogeneity is introduced in the simulations, (ii) how the fields differ between realizations and (iii) to compare the width of the bands to the FEM mesh size. For the band width used here, most bands contain a source and their initial slip resistance consequently ranges between 50 and 250 MPa. Occasionally, a band with a much higher initial slip resistance, on the order of the theoretical strength of the crystal, is present, mimicking the absence of sources in that band. The heterogeneity in properties thus introduced is expected to result in heterogeneous plastic activity, as was demonstrated for a single crystal exhibiting mostly single slip in Wijnen et al. [60]. It was also found in the study that the ability of the model to represent localized slip bands allowed to match experiments more accurately — not only in terms of strain distribution, but also in the slip system that is activated.

The 3D geometry of the region, including the measured thickness distribution and the reconstructed through-thickness grain boundary, is discretized with 64,366 quadratic tetrahedral elements of approximately equal size. The applied boundary conditions are now extracted from the microscale DIC data, in a similar way as was done for the mesoscale case. Thereby, this is considered to be a microscale simulation.

As an initial result, the simulated equivalent strain maps are shown in Fig. 7(f, g) for the two realizations. Obviously, the results are not identical, given the random distribution of sources/initial slip resistance. However, both simulations reveal high strains on the right side of and close to the grain boundary. This compares well to the experiment, although the level of discreteness is less in the simulations. This is due to the practical limitation that the band width l in the simulations cannot be chosen too small, since this would necessitate an excessively fine FE discretization. Additionally, the elevated strain along the top edge of the RoI, which is driven by the presence of the central hole in the '2D' specimen, is also recovered in the simulations.

3.2. Detailed comparison between experiments and simulations: slip system activity fields

While equivalent strain fields are suitable for comparing deformations between experiments and simulations, they only provide insights into the degree of deformation, and yield no insights into locally oriented kinematics. The recently developed ability to extract slip activity fields from the defamation fields measured by DIC, by the SSLIP methodology [38], provides us with a much more detailed basis for comparison between experiments and simulations, see Section 2.4 for a brief explanation.

While all possible slip systems can be considered simultaneously, we decrease the complexity of both the identification and the visualization by only considering the slip systems that are predominantly active in the simulations. As a consequence, there may be a small residual deformation that is not captured by the kinematics of these slip systems, the magnitude of which will also be plotted. The SSLIP methodology is applied here to the front and rear deformation fields. This is visualized in Figs. 8 and 9, for grains 1 and 2 respectively, together with the corresponding slip distributions computed for the respective slip systems in the simulations.

Grain 1 features three dominant slip systems in the simulations, all with the same slip direction: two $\{011\}\langle 11\bar{1}\rangle$ systems (#6 and #10) and one $\{112\}\langle 11\bar{1}\rangle$ system (#18). Application of the SSLIP analysis, considering these three slip systems, to the front and the rear deformation maps, results in the slip activity fields as shown in Fig. 8(a) and (g),

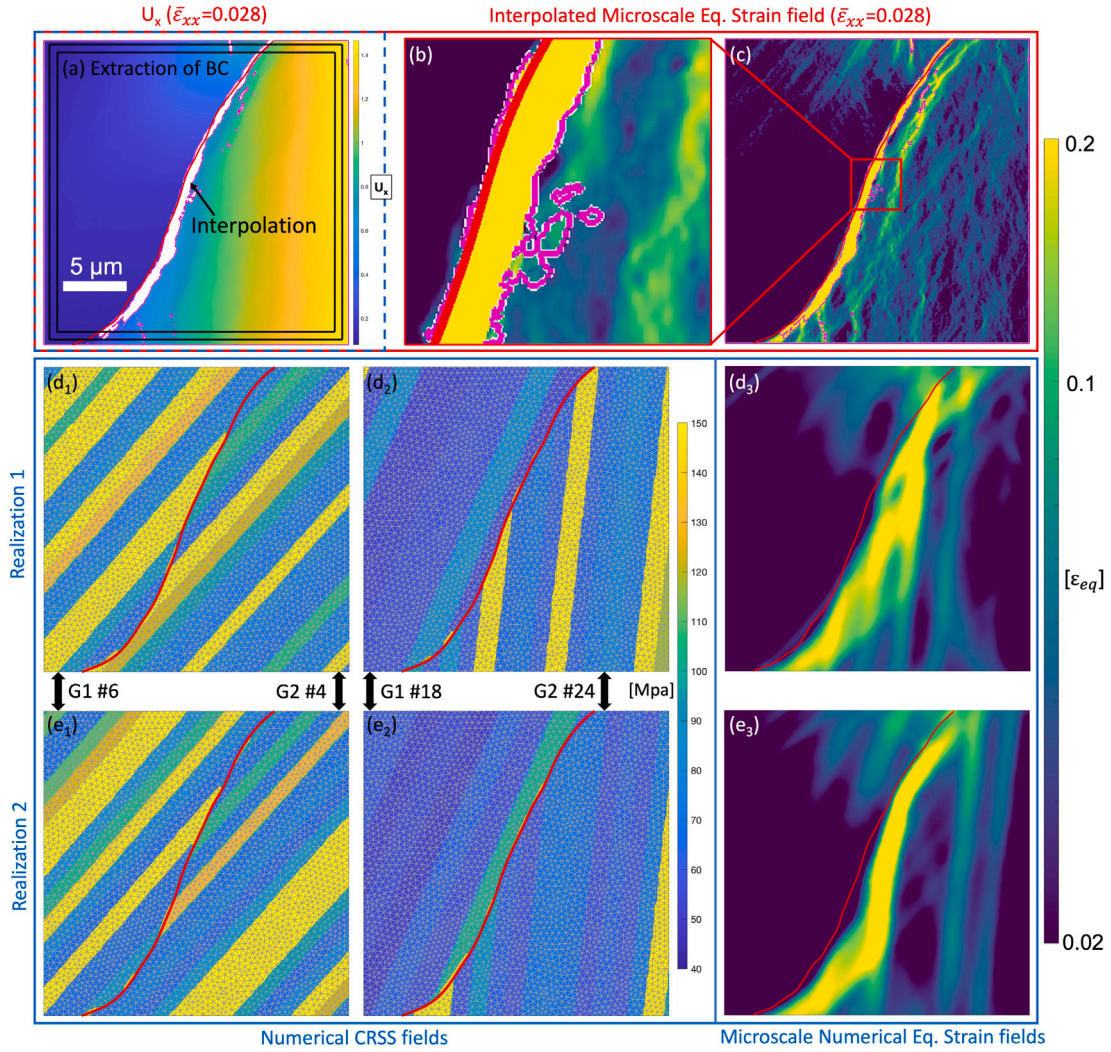

Fig. 7. Microscale experimental deformations, modeling framework and numerical deformations in the microscale region with a single grain boundary, c.f. Fig. 5(b). (a) Map of the x-component of the DIC displacement field. White datapoints in the regions marked by the magenta lines are not successfully correlated. (b) Zoom of the interpolated experimental equivalent strain field as shown in (c). ($d_{1,\ 2}$) For realization 1, CRSS fields for 2 slip systems which are predominantly active, for each grain (G1 and G2) in the simulation, with overlay of the FEM mesh in gray. ($e_{1,\ 2}$) For realization 2, CRSS fields for (the same) 2 slip systems, for each grain in the simulation, with overlay of the FEM mesh in gray. The slip system numbers correspond to those in Figs. 8 and 9. (d_3), (e_3) For realization 1 and 2, 2D equivalent strain fields at the global deformation level of the final experimental increment ($\bar{\varepsilon}_{xx} = 0.028$). In all subfigures, front-side EBSD grain boundaries are drawn as red lines. (For interpretation of the references to color in this figure legend, the reader is referred to the web version of this article.)

respectively. The corresponding equivalent residual strain fields, which contain that part of the deformation which cannot be described by the (combined) kinematics of the considered slip systems, is plotted in Fig. 8(b) and (h), revealing limited activity of other slip system(s) in the top-right corner of grain 1 only. For the simulations, we plot the activity fields of the same slip systems in Fig. 8(c) and (e), for realizations 1 and 2, respectively. Additionally, we show in (d) and (f), for both simulations, the computed equivalent residual strain fields, constructed by combining all other numerical slip system activities into a 2D equivalent strain map. For the simulations, we only show activity maps on the front surface. The full simulation dataset, containing all information in 3D for the 10 realizations, is available to the reader upon request.

For grain 2, the four most active systems in Fig. 9, two $\{011\}\langle 11\bar{1}\rangle$ systems (#4 and #6) and two $\{112\}\langle 11\bar{1}\rangle$ (#14 and #24), are able to nearly completely describe the experimental and numerical deformation. The pairs of systems #4, #24 and #6, #14 both share their slip directions. Aside from the fact that four systems are considered here, Fig. 9 is structured analogous to Fig. 8. Finally, note that a periodic array of parallel lines of slightly increased and decreased slip activity with regular spacing can be observed in some of the experimental slip activity fields, most notably in Figs. 8($a_{2,\ 3}$) and 9(a_2, g_3), which are caused by persistent SEM scanning artefacts that remain after the SEM scanning artefacts correction [29]. These periodic lines should not be confused with actual slip bands. Using a more advanced (custom) SEM scan generator could resolve this.

Experimentally, the validity of the SSLIP identification can be confirmed by noting that the localization bands are aligned to the slip trace of the considered slip system (plotted as a red line in the center of the field), and by evaluation of the residual strain field.

For grain 1, in Fig. 8, both front and rear experimental activity fields show, overall, good alignment between localization bands and theoretical slip traces. The residual does not show clear evidence of additional slip activities, although a minor diffuse residual diffuse strain field remains, which could be low-intensity diffuse plastic slip on non-considered slip systems. The front and rear activity fields are similar, although the rear fields overall do show lower magnitudes as compared to the front. This may be explained by the fact that the rear SEM-DIC images were captured in the unloaded state (after un-mounting the specimen from the tensile stage), which may have induced some

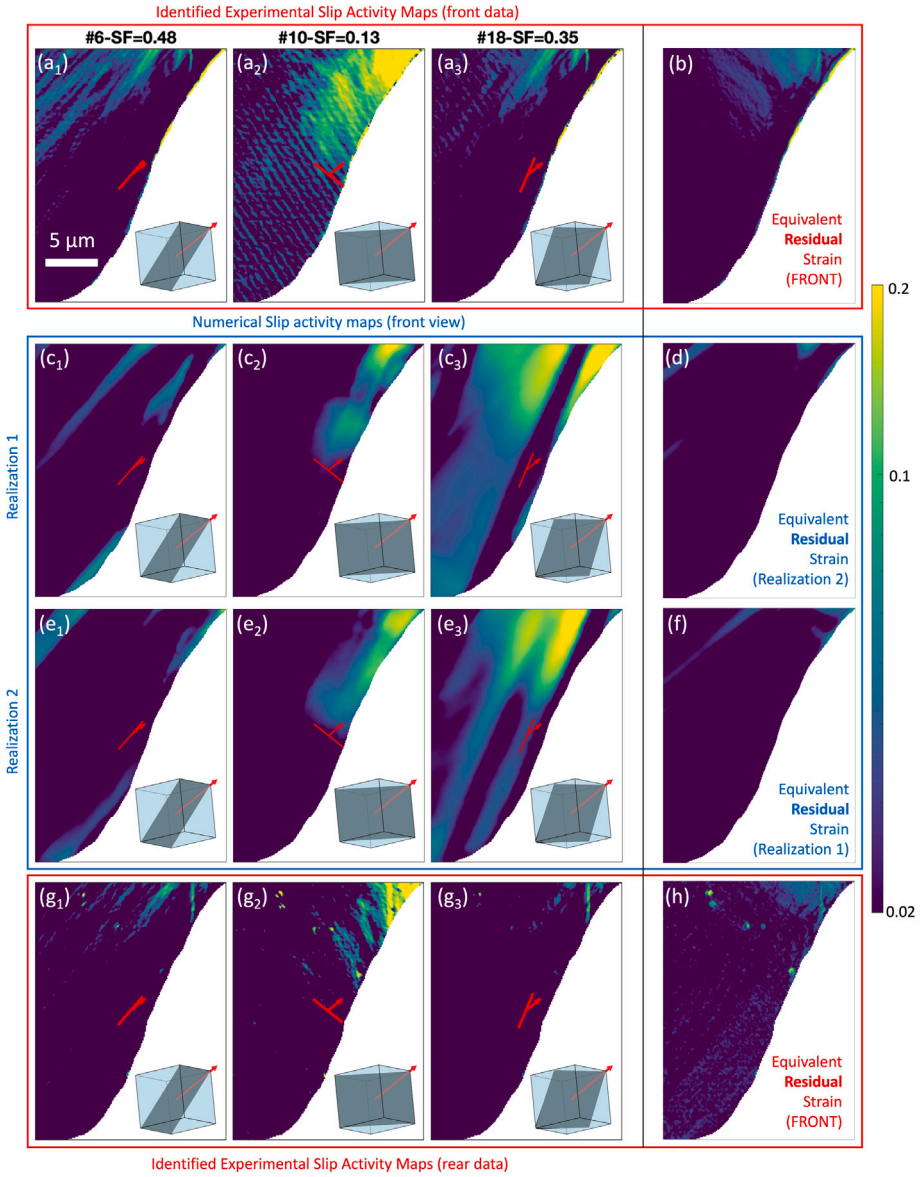

Fig. 8. Comparison of slip system activity fields at $\bar{\varepsilon}_{xx} = 0.028$ of experiments and simulations for grain 1, only considering the three systems that are most active in the simulations. (a) Experimental slip activities on the front surface, with the equivalent residual strain field in (b). (c) and (e) show the numerical slip system activity fields, for realization 1 and 2, respectively. (d) and (f) show the numerical equivalent residual strain field of both realizations. (g) Experimental slip activities on the rear side, with the equivalent residual strain field in (h). The three dominant slip systems are (1) slip system #6 (a $\{011\}\langle 11\bar{1}\rangle$ system with Schmid factor 0.48), (2) slip system #10 (a $\{011\}\langle 11\bar{1}\rangle$ system with Schmid factor 0.13) and (3) slip system #18 (a $\{112\}\langle 11\bar{1}\rangle$ system with Schmid factor 0.35). These three dominant slip systems have the same slip direction. In every activity map, a 3D view of the slip plane and slip direction is plotted inside a rotated cube (which represents the grain orientation). Additionally, the slip plane trace is plotted as a red line, and the in-plane projected slip direction as a red arrow. (For interpretation of the references to color in this figure legend, the reader is referred to the web version of this article.)

reversed plasticity induced by compressive stresses near the central hole, due to the elastic relaxation of the much thicker material away from the hole.

In grain 2, the experimental residual strain fields are much lower than the activity levels of the four slip systems shown. Note that the in-plane slip directions are very close and therefore reduce the certainty of this identification. Additionally, the slip trace validation is not trivial here, since the strongest localization predominantly follows the curved grain boundary. Likely, cross-slip is activated here. Moreover, this strong localization (for which interpolation of the displacement fields was required) appears to occur over both slip directions and over multiple traces, since all four slip systems appear to contribute to this particular localization, although the location of this contribution depends on the slip direction (compare Fig. 8($a_{1,2}$) versus Fig. 8($a_{3,4}$)). Again, the experimental activity fields on front and rear match adequately, providing confidence in the identification.

These high quality experimental slip system activity fields now enable a direct and quantitative comparison with the simulated slip activity fields, with the 'quasi-2D' integrated testing framework providing the inherent precise alignment of the fields. For both grain 1 and grain 2, the experiments and simulations are similar, especially when looking beyond the obvious differences in localization band width and random variation in band intensity between the different simulation realizations, as already seen in Fig. 7. For both grains, on the front and the rear, every active slip system in the simulation is also active in the experiment. Moreover, there is a clear correlation in the overall spatial distribution of slip; this agreement is especially apparent for grain 1, with most activity concentrated near the top of the RoI. In particular, for experiments and simulations, the activity of slip system #6 is located primarily in the top-left corner, whereas slip systems #10 and #18 activate mainly in the top-right corner. Interestingly, slip system #10 has a low Schmid Factor of 0.13, yet is active both in experiment and

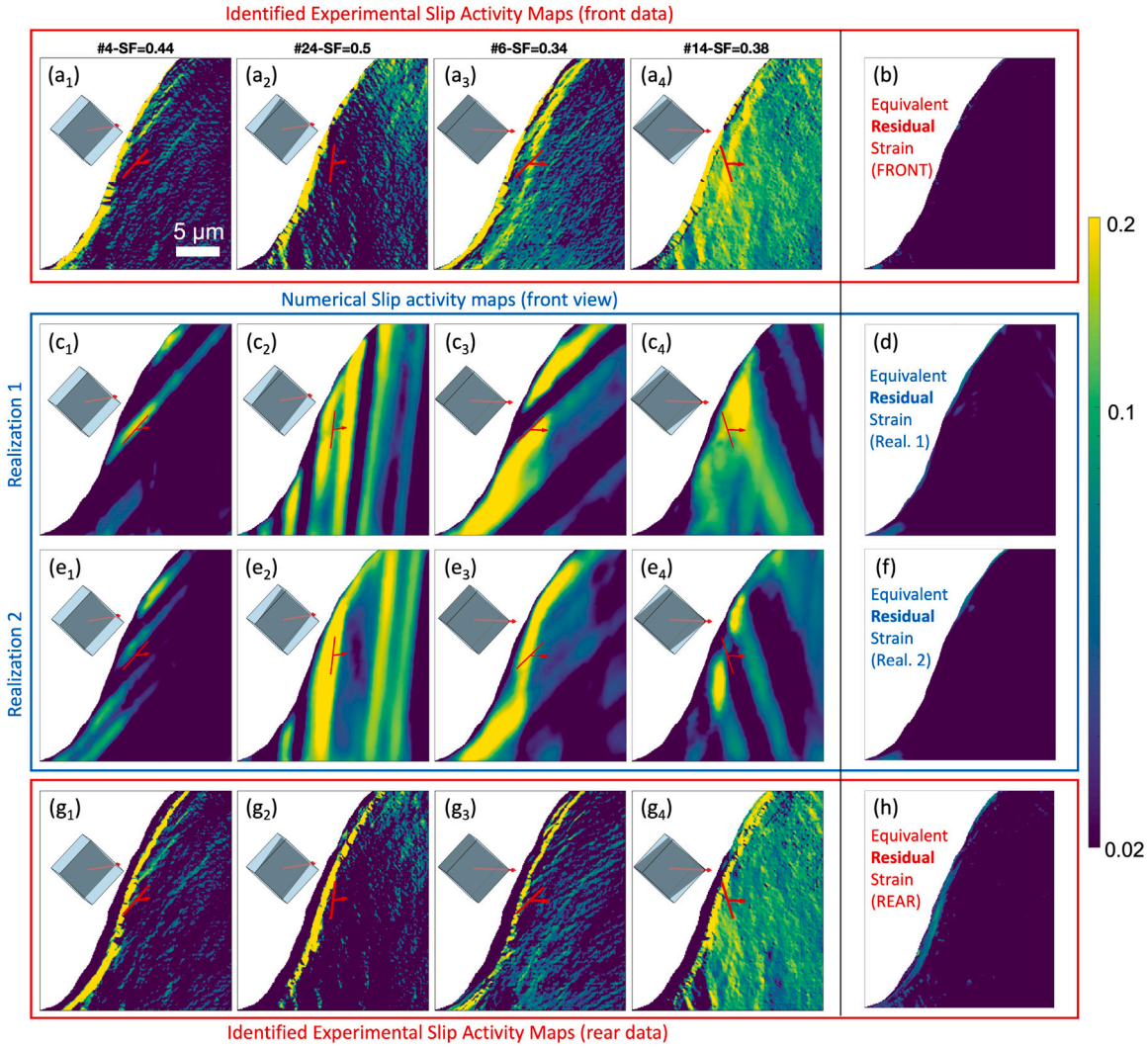

Fig. 9. Comparison of slip system activity fields at $\bar{\varepsilon}_{xx} = 0.028$ of experiments and simulations for grain 2, only considering the four systems that are predominantly active in the simulations. (a) Experimental slip activities on the front side, with the equivalent residual strain field in (b). (c) and (e) show the numerical slip system activity fields, for realization 1 and 2, respectively. (d) and (f) show the numerical equivalent residual strain field of both realizations. (g) Experimental slip activities on the rear side, with the equivalent residual strain field in (h). The four dominant slip systems are (1) slip system #4 (a $\{011\}\langle 11\bar{1}\rangle$ system with Schmid factor 0.44), (2) slip system #24 (a $\{112\}\langle 11\bar{1}\rangle$ system with Schmid factor 0.5), (3) slip system #6 (a $\{011\}\langle 11\bar{1}\rangle$ system with Schmid factor 0.34) and (4) slip system #14 (a $\{112\}\langle 11\bar{1}\rangle$ system with Schmid factor 0.38). Slip systems #4 and #24 share the same slip direction, as do #6 and #14. In every activity map, a 3D view of the slip plane and slip direction is plotted inside a rotated cube (which represents the grain orientation). Additionally, the slip plane trace is plotted as a red line, and the in-plane projected slip direction as a red arrow. (For interpretation of the references to color in this figure legend, the reader is referred to the web version of this article.)

simulations. Its unlikely activation may be (i) due to the presence of the grain boundary, or (ii) caused by the proximity to the hole, which can influence the stress state. In any case, the good match between experiment and simulations demonstrates that the methodology works well.

In grain 2, it is striking that the slip activity of #4 and #6 is located predominantly close to the grain boundary in the simulations and in the (especially rear surface) measurements. In contrast, the experimental and numerical activity of slip system #14 is more spread throughout the grain. Only for slip system #24 the spatial correlation is somewhat less convincing. Finally, as expected from the discrete nature of these simulations, plastic slip proceeds largely within the bands aligned with the slip plane trace, due to the softer properties in that band. Nonetheless, there appears to be a combined activity of multiple slip systems through which the curved localization zone following the grain boundary is accommodated reasonably well (comparable to the experiment). This is most apparent from the simulated equivalent strain fields in Fig. 7(d_3) and (e_3). The fact that the curved localization band is captured reasonably well in the simulations indicates that cross-slip (which is likely active in the experiments) can be captured numerically to some degree using the discrete slip plane model.

In summary, this detailed comparative analysis of slip system activity fields has confirmed that (i) a quantitative comparison, which considers deformation kinematics, is feasible nearby microstructural features such as grain boundaries and (ii) an adequate match can be obtained using a discrete crystal plasticity model. A more comprehensive investigation will follow in future work, where this analysis will be extended to consider the statistics of a larger number of these discrete simulations [60], while also quantifying the difference to employing conventional CP.

4. Case study II: anisotropic martensite plasticity in dual-phase steel

Compared to the single-phase steel considered above, multi-phase steels are typically more challenging, since (i) more microstructural mechanisms are involved, requiring more parameters, (ii) phases such as martensite, bainite, or pearlite have a complex and fine substructure,

compromising the resolution and 3D discretization, and (iii) these complex phases generally show a strongly anisotropic response — see for instance Ref. [61] for the case of martensite. This calls for dedicated modeling approaches. Therefore, this case study focuses on a dual-phase (DP) steel containing ferrite and martensite.

4.1. Experiments: specimen fabrication, characterization & testing

Commercial DP steels have fine microstructures with micrometer sized martensite islands, with sub-micrometer sized variants and laths, severely complicating the fabrication and simulation of a through-thickness microstructure. Therefore, a DP600 grade, with composition 0.092C-1.68Mn- 0.24Si-0.57Cr wt.%, is heat-treated as follows: 20 min austenization at 1000 °C, furnace cooled to 770 °C in 50 min, inter-critically annealed at 770 °C for 50 min, and water quenched to room temperature [29]. This results in a coarse ferritic–martensitic microstructure with a martensite volume fraction of $70 \pm 5\%$.

An area of 500 × 500 μm^2 on the front surface of the fabricated specimen is shown in Fig. 10(b). Since the microstructure is significantly finer as compared to the polycrystalline ferrite specimen, we only performed detailed characterization on the small region indicated with a red square in Fig. 10(b). EBSD and BSE measurements, of the front and the rear, are shown in Fig. 10(a) and (c), respectively. Fig. 10(a_1), (c_1) shows the BSE images, with EBSD grain boundary overlay, obtained after alignment, (a_2), (c_2) shows the EBSD IPF maps, and (a_3), (c_3) shows the ferrite–martensite phase map (computed by thresholding of the EBSD Image Quality (IQ) maps [29]). The thickness map is plotted in Fig. 10(e).

The same InSn speckle patterning approach is used with the same sputter coating parameters as for the ferrite specimen in Section 2.3 [37]. In this case, we only apply a pattern on the front side, to allow for post-mortem EBSD mapping on the rear, as this may provide 3D insights into the plastic deformation field through the analysis of lattice rotations. Next, the specimen is deformed *in-situ* and the small area presented in Fig. 10 is tracked by performing 4096 × 4096 scans of size 48 × 48 μm^2 (for a pixel size of ~12 nm). SEM-DIC is performed with MatchID, using a subset size of 21 pixels at a step size of 1 pixel, employing the same processing steps for strain calculation as described in Section 2.3. Finally, the nanomechanical alignment framework is employed to enable analysis of microstructure-correlated strain fields [29], of which the results are shown in Section 4.3.

4.2. Martensite reconstruction & crystal plasticity modeling

While the dual-phase steel microstructure studied here may be considered as "coarse", the martensite microstructure itself is still rather fine, as observed in the BSE and IPF maps of Fig. 10. Not all martensite grains/variants protrude through the thickness, and their front and rear shapes show strong variations, which prevents an accurate reconstruction of the 3D shape of all grains and variants in the specimen. However, we first address the question whether the crystal orientation of every individual variant must be considered. It is well known that lath martensite has a hierarchical microstructure with a maximum 24 variants in a single Prior Austenite Grain (PAG), described by an Orientation Relationship (OR) [62]. A particularly important feature of this relationship is the habit plane, over which martensite laths grow, resulting in alignment with most lath and variant boundaries. It is known from the literature that plasticity along the habit plane can be promoted in lath martensite [14,20,63–67], through the occurrence of substructure boundary sliding [14,63,64,67], easy habit-plane-aligned crystallographic slip [65], or other mechanisms. Hence, the local habit plane orientation is the key feature for the mechanical behavior of the martensite domains, and this orientation is different for the four possible martensite packets of each PAG, but constant within a packet. Therefore, the martensite microstructure is subjected to a PAG reconstruction in order to identify the packets and their habit plane orientations.

Here, we employ the latest PAG reconstruction routines that have been implemented in the MTEX toolbox in MATLAB [43,44]. First, the best-fitting OR is found by employing the optimization routine of Nyyssönen et al. [68]. Starting with an initial guess of the Kurdjumov–Sachs (KS) OR, all martensite variant-to-variant misorientations are analyzed in tandem to determine the OR. The result is an optimized OR that lies between KS and Nishiyama Wasserman (NW). Subsequently, the optimized OR is used to perform the PAG reconstruction, on the front and the rear separately, using the recently introduced Variant Graph method [69,70]. This is a powerful and fast PAG reconstruction approach that considers all 24 possible parent orientations for each variant, while also performing nearest and next-nearest neighbor analysis. The reconstructed PAG map is inspected for consistency and small PAGs are merged with larger PAGs when their orientation is close, according to procedures similar to those as described by Vermeij et al. [20]. This results in the final PAG maps, for front and rear, as shown in Fig. 10(a_4) and (c_4), respectively.

With the PAG orientations known, the packets and their habit plane orientations can be computed next. Here, we assume the habit plane is a martensite $\{011\}$ plane that is aligned to one of the prior austenite $\{111\}$ planes, an assumption that is at the basis of both the KS and NW OR. We select the correct one of the four prior austenite $\{111\}$ planes by checking which one is closest to any of the 6 martensite $\{011\}$ planes, for every martensite variant. Next, for every packet, which consists of multiple variants with the same habit plane, we compute the so-called "Boundary Sliding Favorability" (BSF), which is a dual to the Schmid Factor (SF), and is defined for the maximum resolved shear stress direction along the $\{111\}$ habit plane: $BSF = cos(\phi) \cdot sin(\phi)$ [20]. This value gives an indication of the likelihood of activation, assuming uniaxial tension, of habit-plane-aligned plasticity, in the form of either (i) substructure boundary sliding, which may occur over various in-plane directions, (ii) (regular) BCC slip within the laths but along the $\{011\}$ habit plane, or (iii) other habit-plane-aligned deformation mechanisms. The packets are plotted, colored according to the BSF, for front and rear, in Fig. 10(d) and (f), respectively, with an overlay of the habit plane trace (black line) in each packet.

To construct a 3D FE discretization, the front and rear microstructure maps, consisting of martensite packets and ferrite grains, are combined with the thickness map as described in Section 2.2, for which the result is plotted in Fig. 10(g). For the ferrite grains, we employ the regular phenomenological crystal plasticity (CP) model as summarized in Appendix A.1. For martensite, we consider two different modeling approaches: 'regular CP' and 'enriched CP'. In both models, plasticity of the BCC martensite laths is defined to occur through crystallographic slip over 12 $\{011\}\langle 11\bar{1}\rangle$ slip systems. To this end, we assign, to each meshed martensite packet in the 3D geometry, the crystal orientation of the most frequently occurring martensite variant in that packet. Simulations where the orientations of the other occurring martensite variants are assigned to the packets are also performed. They showed no significant differences, the reason for which will become apparent later.

For the enriched CP approach, we employ a recently developed reduced laminate model, which captures the softer plasticity over the habit plane, represented by sliding of the martensite substructure boundaries through FCC slip in inter-lath retained austenite films [11,14,20,67,71]. The model is implemented by complementing the 12 BCC slip systems with 3 softer FCC slip systems, of which the slip plane is aligned to the habit plane, representing the interlath retained austenite films. This is implemented through the use of a rule of mixture to take into account the retained austenite volume fraction. Further details, as well as the material parameters, are given in Appendix A.3, while the interested reader is referred to the work of Rezazadeh et al. [14].

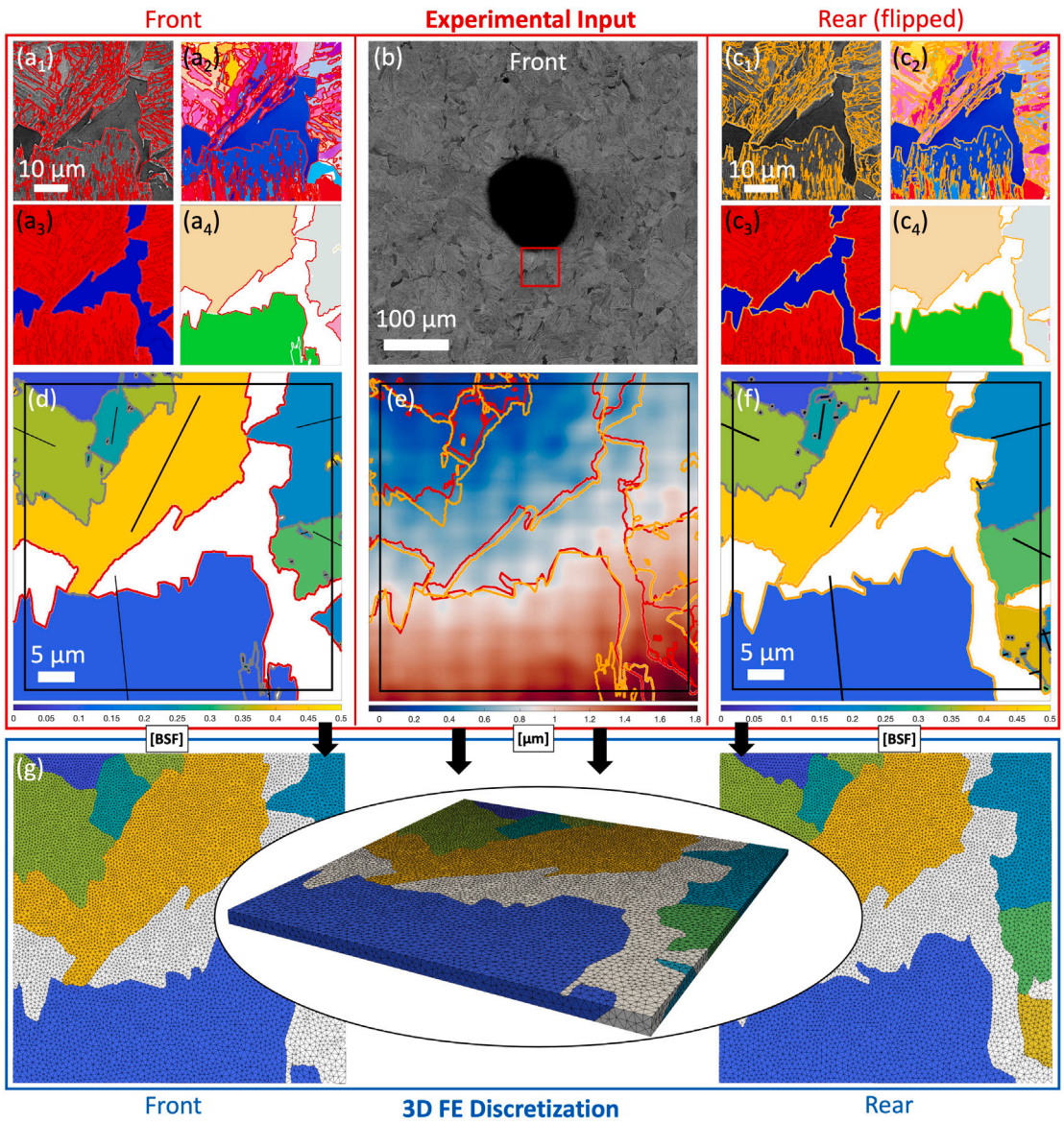

Fig. 10. Experimental microstructure characterization of the ferritic–martensitic sample and extraction of the 3D fine element (FE) discretization for simulations. (a) Detailed microstructure & PAG reconstruction of the front, (b) BSE image of the front side of the sample, with the area of interest indicated in red, and (c) detailed microstructure & PAG reconstruction of the rear. In (a) and (c), (a_1, c_1) show the BSE map with overlay of the EBSD grain boundaries, (a_2, c_2) show the EBSD IPF map, (a_3, c_3) show the ferritic–martensitic phase map retrieved through thresholding of the EBSD IQ map (red for martensite and blue for ferrite) and (a_4, c_4) plots the (IPF) PAG map after PAG reconstruction. In (d) and (f), for front and rear, the packets are plotted, derived after PAG reconstruction and colored according to the habit-plane-derived Boundary Sliding Favorability (BSF). The trace of the habit plane is drawn in black in each packet (with its length scaled to the packet size). (e) Thickness map, with front and rear boundaries superimposed, in red and orange respectively. (g) Constructed 3D mesh of packets and ferrite, with a front view, 3D view and a rear view. (For interpretation of the references to color in this figure legend, the reader is referred to the web version of this article.)

4.3. Comparison of experimental and numerical strain fields

Fig. 11 shows the experimental (a) and numerical (b, c) 2D equivalent von Mises strain fields, for (b) regular and (c) enriched CP, at a global strain level of $\bar{\varepsilon}_{xx} \approx 0.02$ (calculated as the mean strain of the small area). As expected, the softer ferrite grains (denoted with "F" in Fig. 11(a_1) for clarity) accommodate most of the deformation in both experiment and simulation. In the experiment, martensite also deforms plastically, but only in packet 1 (denoted by "P_1" in Fig. 11(a_1)). This packet has a high BSF of 0.43, the highest in the area of interest (see Fig. 10(d, f)), and has a habit plane trace that is roughly aligned to the localization bands in the strain maps. Moreover, the martensite deformation is more concentrated in thin bands than that in ferrite, which can be explained by the occurrence of substructure boundary sliding or by martensite lath slip along the habit plane, constrained within the individual laths. While P_1 deforms over a large area, the predominant path of plasticity is through the ferrite grains from top to bottom, crossing a narrow martensite notch, as shown in detail in the inset in Fig. 11(a_2). Interestingly, even though the narrowest part of the martensite notch is clearly located in packet P_2 (belonging to another PAG) close to the boundary with P_1, the localization percolates completely through P_1, with P_2 not deforming at all. A possible explanation for this is that P_1 is more favorably oriented for slip parallel to the habit plane, which is the 'easier' deformation mode of the packets. This explanation is supported by the difference in BSF, which is only 0.22 for P_2, almost half that of P_1. Fig. 11(a_3) shows the microstructure around the notch, revealing that the orientation of the near-notch martensite laths in P_1 matches well with the three parallel strain bands in P_1, visible in subplot (a_2).

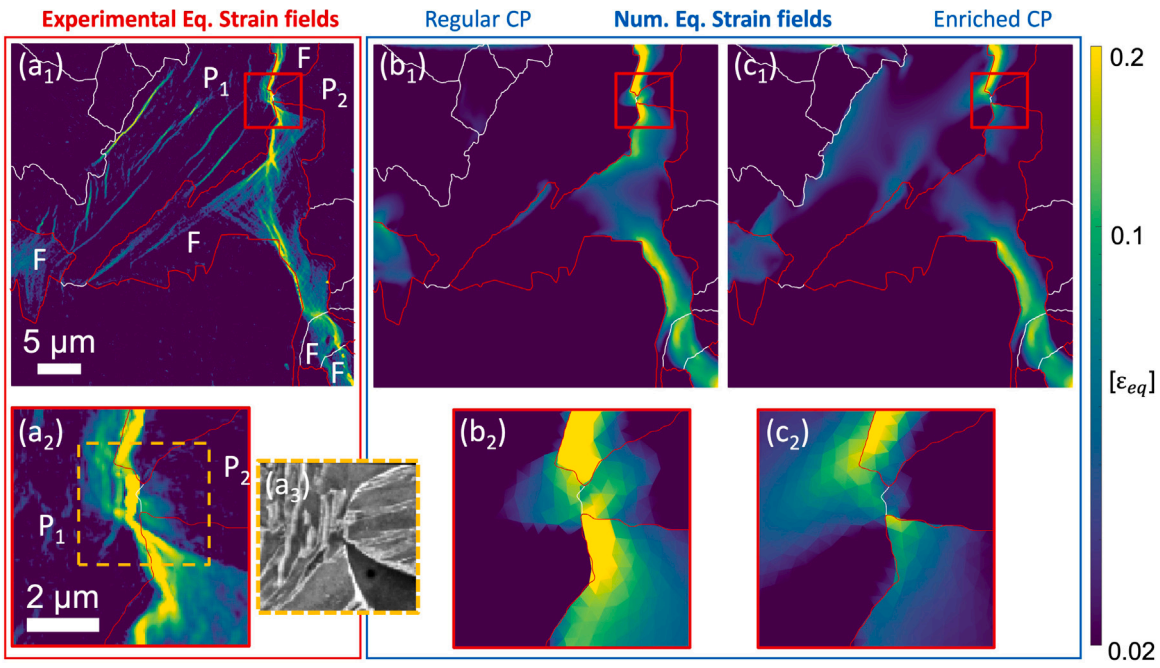

Fig. 11. Deformation fields for (a) experiments and (b, c) simulations of the ferritic–martensitic specimen. (a_1) Experimental equivalent strain field, with packet and ferrite grain boundaries overlaid in white, and phase boundaries in red. Ferrite (F) and two important martensite packets (P_1 and P_2) are indicated. (a_2) Zoom of (a_1) around a martensite notch, with the BSE scan of the microstructure (within orange dashed square) shown in (a_3). (b_1) equivalent strain field of the regular CP simulation, in which only regular BCC slip is employed in martensite, with (b_2) showing the element-averaged strain field near the martensite bridge. (c_1) equivalent strain field of the enriched CP simulation, in which, besides regular BCC slip, softer austenite slip systems along the habit plane are incorporated in each martensite packet, with (c_2) showing the element-averaged strain field at the martensite bridge. (For interpretation of the references to color in this figure legend, the reader is referred to the web version of this article.)

Fig. 11(b_1) shows the equivalent strain field resulting from the regular CP framework (employing only regular BCC plasticity for martensite), with the inset (Fig. 11(b_2)) again focusing on the martensite notch, here plotting the element-averaged equivalent strains. The regular CP simulation shows an adequate agreement within the ferrite, but fails to reproduce the experimentally observed activity in packet P_1. At the notch, the strains percolate through both packets, but mainly through the thinner P_2 packet, as can be expected from a simulation that ignores the habit-plane related plasticity mechanism. In contrast, the habit-plane enriched CP simulation in Fig. 11(c) reveals significant plasticity in a large part of packet P_1, similar to the experiments. Moreover, at the notch, the plastic band originating from the ferrite grain above penetrates into packet P_1, while clearly avoiding P_2 (Fig. 11(c_2)). This reveals a clear agreement with the experiment, although the precise deformation pattern in packet P_1 to connect with the ferrite grain below differs. Additionally, the martensite deforms in a more localized manner in the experiment as compared to the simulation. Finally, the ferrite strains in the enriched CP are marginally lower, which can be explained by the fact that both simulations operate under equal in-plane mean deformation, with the enriched CP accommodating some plasticity in the martensite packet P_1.

To conclude, by adopting a recently introduced substructure-enriched modeling approach incorporating the correct plastic anisotropy in martensite, we found a convincing experimental–numerical match. However, the match will improve even more if the habit plane plasticity mechanism can also be 'discretized' in the simulation, as was done for the ferrite in the case study I. Nonetheless, it was shown that through these integrated experimental–numerical studies, there is great potential for validation or falsification of a numerical model and/or identification of critical parameters of otherwise hard-to-identify material model parameters, such as the martensite–austenite phase contrast. Moreover, further deformation of this specimen can lead to damage in the martensite notch, providing opportunities for validation of damage indicators or directly modeling damage through the implementation of softening. Both of these topics are outside the scope of this paper and will be addressed in future work.

5. Conclusions

We proposed a novel 'quasi-2D' integrated experimental–numerical testing approach in which the specimens may have a significant microstructural complexity, well beyond traditional micro-deformation experiments such as micro-pillar compression tests. The full 3D microstructure can be determined, which is not the case in bulk experiments. To this end, (steel) specimens are fabricated with a thickness in the order of micrometers over a large (mesoscale) area, of hundreds of micrometers in size. The resulting through-thickness microstructure can readily be discretized and simulated in 3D, while the specimens can relatively easily (as compared to micro-deformation tests) be tested *in-situ* for high-resolution deformation field measurements. This approach provides the opportunity for detailed, quantitative and direct comparisons between experiments and advanced simulations.

The '2D' testing framework consists of the following experimental/numerical methodological steps:

- **Specimen fabrication:** relatively straightforward fabrication of ultra-thin specimens, with close to through-thickness microstructure around a central hole, by performing routine twin-jet electropolishing on a (steel) sample plate, with the great advantage that the specimen can easily be handled manually and tested in a standard *in-situ* tensile tester.
- **Microstructure & 3D geometry:** front and rear microstructure characterization by, e.g., Backscatter Electron (BSE) imaging and Electron Backscatter Diffraction (EBSD), thickness profile measurement of the full area by front and rear optical profilometry and subsequent alignment of all data.
- **Simulation setup:** generation of a 3D geometry and microstructure conforming Finite Element (FE) mesh, by combination of measured front and rear microstructure with the thickness map.
- **In-situ testing:** *in-situ* Scanning Electron Microscopy based Digital Image Correlation (SEM-DIC) tensile-testing using a high-quality mesoscale and/or nanoscale InSn DIC speckle pattern,

with subsequent alignment for microstructure-correlated strain fields.

- **Simulating the experiment:** conducting FE simulations with boundary conditions that have been extracted from the experimental deformation fields at the edges of the region of interest. Any material model can be used, such as regular Crystal Plasticity (CP) or extensions to it.
- **1–to–1 Experimental/Numerical comparison:** deformation maps of experiments and simulations are assessed on aligned grids. The comparison can be done not only using strain maps, but also through slip system activity fields that are naturally available from crystal plasticity simulations and which can be generated experimentally using the Slip Systems Local Identification of Plasticity (SSLIP) method, as recently proposed in [38].

All the steps of the framework were first explained and demonstrated on an Interstitial-Free (IF) ferritic steel with a polycrystalline microstructure. At the mesoscale of multiple grains, through employment of a conventional CP modeling approach, the experimental deformation map could be replicated reasonably well. The embedded high-resolution microscale strain maps revealed heterogeneous plastic slip at various microstructural features, which could not be captured by the simple CP model.

In case study I, we further explored the IF steel at the microscale, by performing simulations on a specific region around a grain boundary, employing a recently introduced discrete CP modeling approach. The application of SSLIP, on both the front and the rear, revealed unique insights into the comparability of the kinematics between experiments and simulations. An unprecedented match was found, providing confidence in the 'quasi-2D' integrated experimental-numerical analysis.

Case study II involved a more challenging material: a dual-phase steel with a coarse ferritic–martensitic microstructure. Here, our focus was on a small region for which most of the methodology steps could be repeated without any adaptations. Only the fine and complex hierarchical substructure of the martensite packets required a reconstruction of the prior austenite grains for the identification of the packets and their corresponding habit planes. 3D meshing was then performed using the front and rear maps of the ferrite grains and martensite packets plus the thickness distribution. Experimental equivalent strain maps revealed pronounced ferrite plasticity, along with one particularly active martensite packet, which was explained by a habit-plane related soft martensite deformation mechanisms. Indeed, modeling the martensite by conventional BCC crystal plasticity yielded a poor agreement to the experimentally established martensite activity. Therefore, a recently proposed substructure-enriched CP model was employed, in which a soft plasticity mechanism along the habit plane is incorporated, resulting in a superior comparison.

The proposed methodology does come with some limitations that may be solved with future extensions. First, the experimental-numerical stress–strain curves were not compared here, since the cross-section of the thin region of interest is less than 1% of the full sample cross-section. However, we believe local stress levels can indirectly be measured to achieve an absolute calibration of CP parameters. By assuming knowledge of the (anisotropic) elasticity parameters, elastic behavior can act as a local force sensor, especially as the thicker specimen area may not deform fully plastically. This approach was demonstrated successfully by Ruybalid et al. who also applied boundary conditions based on DIC data [59]. Second, lattice rotations can be measured post-mortem with EBSD, provided one specimen surface has no DIC speckle pattern (e.g. by post-mortem removal), yielding extra data for experimental-numerical validation. The power of adding lattice rotations in the experimental-numerical comparison was, e.g., shown by Tasan et al. [12,13]. Finally, for the specimen thickness demonstrated here, the methodology is limited to microstructures with grain sizes down to ~500 nm, based on the need for through-thickness grains. Smaller microstructures would require further optimization of the specimen thickness and EBSD and DIC resolution.

In summary, we showed that the 'quasi-2D' integrated experimental-numerical approach presented here accurately reproduces experimental observations through representative 3D numerical simulations, even for complex microstructures. Thereby, the notorious problem of the unknown 3D microstructure in bulk samples is avoided, while retaining sufficient in-plane microstructural complexity to be able to study the interplay between distinct deformation mechanisms. As such, the 'quasi-2D' integrated testing method holds great potential for validation or falsification of any kind of material model, for identification of material parameters of complex material models and/or alloys, and for detailed experimental/numerical comparison of (even) more complex micro-deformation mechanisms such as damage and fracture.

CRediT authorship contribution statement

T. Vermeij: Conceptualization, Methodology, Software, Investigation (Experiments), Writing – original draft, Visualization. **J. Wijnen:** Methodology, Software, Investigation (Simulations), Writing – review & editing, Visualization. **R.H.J. Peerlings:** Conceptualization, Methodology, Writing – review & editing, Supervision, Funding acquisition. **M.G.D. Geers:** Methodology, Resources, Writing – review & editing, Supervision, Funding acquisition. **J.P.M. Hoefnagels:** Conceptualization, Methodology, Resources, Writing – review & editing, Supervision, Funding acquisition.

Declaration of competing interest

The authors declare that they have no known competing financial interests or personal relationships that could have appeared to influence the work reported in this paper.

Acknowledgments

The authors acknowledge contributions of Jorn Verstijnen, Rick van Eert and Marc van Maris for discussions and experimental support. This research was carried out as part of the "UNFAIL" project, under project numbers S17012a and S17012b in the framework of the Partnership Program of the Materials innovation institute M2i (www.m2i.nl) and the Netherlands Organization for Scientific Research (http://www.nwo.nl).

Appendix. Simulation details

A.1. Conventional crystal plasticity

The conventional (phenomenological) Crystal Plasticity (CP) model employed in this work is founded in finite deformation theory. The deformation gradient tensor $\mathbf{F}$ is multiplicatively decomposed into elastic ($\mathbf{F}_e$) and plastic ($\mathbf{F}_p$) contributions:

$$\mathbf{F} = \mathbf{F}_e \cdot \mathbf{F}_p \tag{A.1}$$

The elastic contribution translates into the Second Piola–Kirchhoff stress tensor $\mathbf{S}_e$, through

$$\mathbf{S}_e = \tfrac{1}{2}\mathbb{C} : (\mathbf{F}_e^T \cdot \mathbf{F}_e - \mathbf{I}), \tag{A.2}$$

where $\mathbb{C}$ is the fourth-order elasticity tensor and : denotes a double contraction. The rate of plastic deformation is described by the plastic velocity gradient tensor $\mathbf{L}_p$:

$$\mathbf{L}_p = \dot{\mathbf{F}}_p \cdot \mathbf{F}_p^{-1} = \sum_{\alpha=1}^{N} \dot{\gamma}^\alpha \vec{s}^\alpha \otimes \vec{n}^\alpha, \tag{A.3}$$

Table A.1
Model parameters for ferrite.
Source: Taken from [23].

Model parameter	Symbol	Value
Initial slip resistance	s_0	15 MPa
Saturation slip resistance	s_∞	250 MPa
Initial hardening rate	h_0	120 GPa
Hardening exponent	a	17.5
Latent hardening coefficient	q_n	1.4
Slip rate sensitivity	m	0.02
Reference slip rate	$\dot{\gamma}_0$	0.01 s^{-1}
Elastic constant	C_{11}	233.5 GPa
Elastic constant	C_{12}	135.5 GPa
Elastic constant	C_{44}	118.0 GPa

Table A.2
Material parameters for dual-phase steel used in the regular and enriched CP models.

Model parameter	Symbol	Ferrite	Martensite	Austenite
Initial slip resistance	s_0	112.1 MPa	510 MPa	265 MPa
Saturation slip resistance	s_∞	224.8 MPa	2000 MPa	340 MPa
Initial hardening rate	h_0	8.212 GPa	1.5 GPa	0.25 GPa
Hardening exponent	a	1.32	1.5	1.5
Latent hardening coefficient	q_n	1.0	1.0	1.0
Slip rate sensitivity	m	0.05	0.05	0.05
Reference slip rate	$\dot{\gamma}_0$	0.01 s^{-1}	0.01 s^{-1}	0.01 s^{-1}
Volume fraction	ϕ	–	–	0.05
Elastic constant	C_{11}	233.5 GPa	283.0 GPa	–
Elastic constant	C_{12}	135.5 GPa	121.0 GPa	–
Elastic constant	C_{44}	118.0 GPa	81.0 GPa	–

where $\dot{\gamma}^\alpha$ indicates the shear rate on slip system α, which has $\vec{n}^\alpha$ as slip plane normal and $\vec{s}^\alpha$ as a slip direction, while N is the number of slip systems. For polycrystalline ferrite BCC case, we use 12 $\{110\}\langle 111\rangle$ and 12 $\{112\}\langle 111\rangle$ slip systems in each grain. For regular BCC martensite plasticity, only the $\{110\}\langle 111\rangle$ slip systems are employed. A standard visco-plastic CP approach is employed in which the shear rate on each slip system is determined by a resolved shear stress τ^α and a flow resistance s^α [7]:

$$\dot{\gamma}^\alpha = \dot{\gamma}_0 \left(\frac{|\tau^\alpha|}{s^\alpha} \right)^{\frac{1}{r}} \operatorname{sign}(\tau^\alpha), \tag{A.4}$$

where $\dot{\gamma}_0$ is the reference shear rate and r is the rate-sensitivity exponent. The resolved shear stress on a slip system in the intermediate configuration is calculated as

$$\tau^\alpha = \vec{s}^\alpha \cdot \mathbf{F}_e^T \cdot \mathbf{F}_e \cdot \mathbf{S}_e \cdot \vec{n}^\alpha. \tag{A.5}$$

The slip resistance of a slip system has an initial value s_0^α and evolves asymptotically to s_∞^α:

$$\dot{s}^\alpha = h_0 \left(1 - \frac{s^\alpha}{s_\infty^\alpha} \right)^a \sum_{\beta=1}^{N} q^{\alpha\beta} |\dot{\gamma}^\beta|, \tag{A.6}$$

where h_0 and α are hardening parameters. The adopted material parameters are given in Table A.1.

All finite element models in this work are implemented in the form of Fortran user subroutines in the commercial finite element package *Msc.Marc*. The update of state variables $\mathbf{F}_p$ and s is done implicitly via a trapezoidal integration scheme.

A.2. Discrete microscale crystal plasticity

The discrete slip plane model introduces heterogeneity to the plastic slip by a random variation of the initial slip resistance, mimicking the presence (or absence) of dislocation sources and obstacles. Its formulation is based on a relative displacement (slip) distribution associated with each atomic slip line and step direction. For numerical simulations, however, these discrete slip the planes are collected in bands and it is assumed that the response of the band is governed by the weakest slip lane within it - i.e. that slip plane with the lowest initial slip assistance. This renders the model very similar to the conventional CP, albeit with material properties (initial slip resistance) which vary in space according to the bands associated with each slip system.

Formulated in terms of a shear rate within the band, the slip law reads

$$\dot{\gamma}^\alpha = \frac{\dot{v}_0}{l} \left(\frac{|\tau^\alpha|}{s^\alpha} \right)^{\frac{1}{r}} \operatorname{sign}(\tau^\alpha), \tag{A.7}$$

where $\dot{v}_0$ is a reference velocity and l is the width of the band. The evolution of the slip resistance with initial value s_0^α is given by

$$\dot{s}^\alpha = k_0 l \left(1 - \frac{s^\alpha}{s_\infty^\alpha} \right)^a \sum_{\beta=1}^{N} q^{\alpha\beta} |\dot{\gamma}^\beta|, \tag{A.8}$$

where k_0 is the initial hardening rate. For a more detailed treatment of the model the reader is referred to Wijnen et al. [10].

A.3. Reduced martensite laminate model

The reduced laminate model for lath martensite assumes that thin films of retained austenite are present between the martensite laths, i.e. parallel to the habit plane, and that plastic deformation of these films presents an additional, softer deformation mechanism parallel to the habit plane. This mechanism is incorporated by adding its contribution to the flow rule of Eq. (A.3), as follows:

$$\mathbf{L}_p = \sum_{\alpha=1}^{12} \dot{\gamma}_{\alpha'}^\alpha \, \vec{s}_{\alpha'}^\alpha \otimes \vec{n}_{\alpha'}^\alpha \qquad + \varphi \sum_{\alpha=1}^{3} \dot{\gamma}_\gamma^\alpha \, \vec{s}_\gamma^\alpha \otimes \vec{n}_\gamma^\alpha \tag{A.9}$$

In this expression, the first term, with slip systems α', represents plastic deformation of the laths, whereas the second, non standard term represents the additional plastic mechanism of flow of the interlath retained austenite, through slip systems γ. The austenite volume fraction φ appears in this term to account for the fact that the additional mechanism is active only in the austenite films; it is set at 5% for this work [14]. Only the three $\{111\}\langle 110\rangle_\gamma$ FCC austenite slip systems which have their slip plane aligned to the $(011)_{\alpha'}$ habit plane of each variant are considered in the additional contribution. This is based on the reasoning that, due to the morphology of the laths and the existing OR between austenite and martensite, the activity of Out-Of-Habit-Plane slip systems in austenite films is constrained by the laths, and will therefore not contribute to the softer habit plane sliding mechanism. The slip rates $\dot{\gamma}_{\alpha'}$ and $\dot{\gamma}_\gamma$ in both terms of Eq. (A.9) are governed by the slip law (Eq. (A.4)), albeit with different parameters for the lath and austenite films. The two parts of the model are however driven by the same stress tensor — which is resolved to the individual slip systems through Eq. (A.5). The slip resistances are governed by the hardening law (Eq. (A.8)), again with different parameters for the two phases. finally, no interaction (latent hardening) is assumed between the two phases.

The adopted model parameters for the regular and enriched CP models can be found in Table A.2. For more details, the reader is referred to the work of Rezazadeh et al. [14].

References

[1] I. Gutierrez-Urrutia, D. Raabe, Dislocation and twin substructure evolution during strain hardening of an Fe–22 wt% Mn–0.6 wt% C TWIP steel observed by electron channeling contrast imaging, Acta Mater. 59 (16) (2011) 6449–6462.
[2] C.C. Tasan, M. Diehl, D. Yan, M. Bechtold, F. Roters, L. Schemmann, C. Zheng, N. Peranio, D. Ponge, M. Koyama, K. Tsuzaki, D. Raabe, An overview of dual-phase steels: Advances in microstructure-oriented processing and micromechanically guided design, Annu. Rev. Mater. Res. 45 (1) (2015) 391–431.
[3] R. Badji, M. Bouabdallah, B. Bacroix, C. Kahloun, B. Belkessa, H. Maza, Phase transformation and mechanical behavior in annealed 2205 duplex stainless steel welds, Mater. Character. 59 (4) (2008) 447–453.

[4] T. Seshacharyulu, S.C. Medeiros, W.G. Frazier, Y.V.R.K. Prasad, Microstructural mechanisms during hot working of commercial grade Ti–6Al–4V with lamellar starting structure, Mater. Sci. Eng. A 325 (1–2) (2002) 112–125.

[5] E.P. George, W.A. Curtin, C.C. Tasan, High entropy alloys: A focused review of mechanical properties and deformation mechanisms, Acta Mater. 188 (2020) 435–474.

[6] F. Maresca, W.A. Curtin, Mechanistic origin of high strength in refractory BCC high entropy alloys up to 1900K, Acta Mater. 182 (2020) 235–249.

[7] F. Roters, M. Diehl, P. Shanthraj, P. Eisenlohr, C. Reuber, S.L. Wong, T. Maiti, A. Ebrahimi, T. Hochrainer, H.O. Fabritius, S. Nikolov, M. Friák, N. Fujita, N. Grilli, K.G.F. Janssens, N. Jia, P.J.J. Kok, D. Ma, F. Meier, E. Werner, M. Stricker, D. Weygand, D. Raabe, DAMASK – the Düsseldorf advanced material simulation kit for modeling multi-physics crystal plasticity, thermal, and damage phenomena from the single crystal up to the component scale, Comput. Mater. Sci. 158 (2018) (2019) 420–478.

[8] J.R. Mianroodi, P. Shanthraj, C. Liu, S. Vakili, S. Roongta, N.H. Siboni, N. Perchikov, Y. Bai, B. Svendsen, F. Roters, et al., Modeling and simulation of microstructure in metallic systems based on multi-physics approaches, Comput. Mater. 8 (1) (2022) 1–15.

[9] C. Liu, F. Roters, D. Raabe, Finite strain crystal plasticity-phase field modeling of twin, dislocation, and grain boundary interaction in hexagonal materials, Acta Mater. 242 (2023) 118444.

[10] J. Wijnen, R.H.J. Peerlings, J.P.M. Hoefnagels, M.G.D. Geers, A discrete slip plane model for simulating heterogeneous plastic deformation in single crystals, Int. J. Solids Struct. 228 (2021) 10.

[11] V. Rezazadeh, R.H.J. Peerlings, F. Maresca, J.P.M. Hoefnagels, M.G.D. Geers, An effective anisotropic visco-plastic model dedicated to high contrast ductile laminated microstructures: Application to lath martensite substructure, 2022, arXiv:2211.09754.

[12] C.C. Tasan, M. Diehl, D. Yan, C. Zambaldi, P. Shanthraj, F. Roters, D. Raabe, Integrated experimental–simulation analysis of stress and strain partitioning in multiphase alloys, Acta Mater. 81 (2014) 386–400.

[13] C.C. Tasan, J.P.M. Hoefnagels, M. Diehl, D. Yan, F. Roters, D. Raabe, Strain localization and damage in dual phase steels investigated by coupled in-situ deformation experiments and crystal plasticity simulations, Int. J. Plast. 63 (2014) 198–210.

[14] V. Rezazadeh, R.H.J. Peerlings, T. Vermeij, J.P.M. Hoefnagels, F. Maresca, M.G.D. Geers, Extensive anisotropic lath martensite plasticity in dual-phase steels: A numerical-experimental investigation, 2022, arXiv:2211.08331.

[15] M. Diehl, D. An, P. Shanthraj, S. Zaefferer, F. Roters, D. Raabe, Crystal plasticity study on stress and strain partitioning in a measured 3D dual phase steel microstructure, Phys. Mesomech. 20 (3) (2017) 311–323.

[16] Z. Zhang, D. Lunt, H. Abdolvand, A.J. Wilkinson, M. Preuss, F.P.E. Dunne, Quantitative investigation of micro slip and localization in polycrystalline materials under uniaxial tension, Int. J. Plast. 108 (2018) 88–106.

[17] A. Guery, F. Hild, F. Latourte, S. Roux, Slip activities in polycrystals determined by coupling DIC measurements with crystal plasticity calculations, Int. J. Plast. 81 (2016) 249–266.

[18] Q. Shi, F. Latourte, F. Hild, S. Roux, Backtracking depth-resolved microstructures for crystal plasticity identification—part 1: Backtracking microstructures, JOM 69 (12) (2017) 2810–2818.

[19] K. Thool, A. Patra, D. Fullwood, K.V.M. Krishna, D. Srivastava, I. Samajdar, The role of crystallographic orientations on heterogeneous deformation in a zirconium alloy: a combined experimental and modeling study, Int. J. Plast. 133 (2020) 102785.

[20] T. Vermeij, C.J.A. Mornout, V. Rezazadeh, J.P.M. Hoefnagels, Martensite plasticity and damage competition in dual-phase steel: A micromechanical experimental-numerical study, Acta Mater. 254 (2023) 119020.

[21] G. Dehm, B.N. Jaya, R. Raghavan, C. Kirchlechner, Overview on micro- and nanomechanical testing: New insights in interface plasticity and fracture at small length scales, Acta Mater. 142 (2018) 248–282.

[22] P. Lin, Z. Liu, Z. Zhuang, Numerical study of the size-dependent deformation morphology in micropillar compressions by a dislocation-based crystal plasticity model, Int. J. Plast. 87 (2016) 32–47.

[23] C. Du, F. Maresca, M.G.D. Geers, J.P.M. Hoefnagels, Ferrite slip system activation investigated by uniaxial micro-tensile tests and simulations, Acta Mater. 146 (2018) 314–327.

[24] D.E. Hurtado, M. Ortiz, Surface effects and the size-dependent hardening and strengthening of nickel micropillars, J. Mech. Phys. Solids 60 (8) (2012) 1432–1446.

[25] P.A. Shade, R. Wheeler, Y.S. Choi, M.D. Uchic, D.M. Dimiduk, H.L. Fraser, A combined experimental and simulation study to examine lateral constraint effects on microcompression of single-slip oriented single crystals, Acta Mater. 57 (15) (2009) 4580–4587.

[26] L. Chen, T.E.J. Edwards, F. Di Gioacchino, W.J. Clegg, F.P.E. Dunne, M. Pham, Crystal plasticity analysis of deformation anisotropy of lamellar TiAl alloy: 3D microstructure-based modelling and in-situ micro-compression, Int. J. Plast. 119 (2019) 344–360.

[27] S. Breumier, S. Sao-Joao, A. Villani, M. Lévesque, G. Kermouche, High strain rate micro-compression for crystal plasticity constitutive law parameters identification, Mater. Des. 193 (2020) 108789.

[28] M. Bertin, C. Du, J.P.M. Hoefnagels, F. Hild, Crystal plasticity parameter identification with 3D measurements and integrated digital image correlation, Acta Mater. 116 (2016) 321–331.

[29] T. Vermeij, J.A.C. Verstijnen, T.J.J. Ramirez y Cantador, B. Blaysat, J. Neggers, J.P.M. Hoefnagels, A nanomechanical testing framework yielding front & rear-sided, high-resolution, microstructure-correlated SEM-DIC strain fields, Exp. Mech. 62 (2022) 1625–1646.

[30] C. Du, J.P.M. Hoefnagels, L.I.J.C. Bergers, M.G.D. Geers, A uni-axial nano-displacement micro-tensile test of individual constituents from bulk material, Exp. Mech. 57 (8) (2017) 1249–1263.

[31] C. Motz, T. Schöberl, R. Pippan, Mechanical properties of micro-sized copper bending beams machined by the focused ion beam technique, Acta Mater. 53 (15) (2005) 4269–4279.

[32] A. Zeghadi, S. Forest, A.F. Gourgues, O. Bouaziz, Ensemble averaging stress–strain fields in polycrystalline aggregates with a constrained surface microstructure—part 2: Crystal plasticity, Phil. Mag. 87 (8–9) (2007) 1425–1446.

[33] M. Diehl, P. Shanthraj, P. Eisenlohr, F. Roters, Neighborhood influences on stress and strain partitioning in dual-phase microstructures, Meccanica 51 (2) (2016) 429–441.

[34] M.A. Groeber, B.K. Haley, M.D. Uchic, D.M. Dimiduk, S. Ghosh, 3D reconstruction and characterization of polycrystalline microstructures using a FIB–SEM system, Mater. Character. 57 (4–5) (2006) 259–273.

[35] Q. Shi, F. Latourte, F. Hild, S. Roux, Backtracking depth-resolved microstructures for crystal plasticity identification—part 2: identification, JOM 69 (12) (2017) 2803–2809.

[36] Z. Zhao, M. Ramesh, D. Raabe, A.M. Cuitino, R. Radovitzky, Investigation of three-dimensional aspects of grain-scale plastic surface deformation of an aluminum oligocrystal, Int. J. Plast. 24 (12) (2008) 2278–2297.

[37] J.P.M. Hoefnagels, M.P.F.H.L. van Maris, T. Vermeij, One-step deposition of nano-to-micron-scalable, high-quality digital image correlation patterns for high-strain in-situ multi-microscopy testing, Strain 55 (6) (2019) e12330, e12330 STRAIN-1507.R1.

[38] T. Vermeij, R.H.J. Peerlings, M.G.D. Geers, J.P.M. Hoefnagels, Automated identification of slip system activity fields from digital image correlation data, Acta Mater. 243 (2023) 118502.

[39] A. Marano, L. Gélébart, S. Forest, FFT-based simulations of slip and kink bands formation in 3D polycrystals: Influence of strain gradient crystal plasticity, J. Mech. Phys. Solids 149 (2021) 104295.

[40] M.T. Tzini, J.S. Aristeidakis, P.I. Christodoulou, A.T. Kermanidis, G.N. Haidemenopoulos, D. Krizan, Multi-phase field modeling in TRIP steels: Distributed vs. average stability and strain-induced transformation of retained austenite, Mater. Sci. Eng. A 833 (2022) 142341.

[41] M. Diehl, M. Wicke, P. Shanthraj, F. Roters, A. Brueckner-Foit, D. Raabe, Coupled crystal plasticity–phase field fracture simulation study on damage evolution around a void: pore shape versus crystallographic orientation, JOM 69 (5) (2017) 872–878.

[42] D.B. Williams, C.B. Carter, Transmission Electron Microscopy, second ed., Springer, 2009.

[43] F. Bachmann, R. Hielscher, H. Schaeben, Texture analysis with MTEX – free and open source software toolbox, in: Texture and Anisotropy of Polycrystals III, in: Solid State Phenomena, vol. 160, Trans Tech Publications Ltd, 2010, pp. 63–68.

[44] R. Hielscher, H. Schaeben, A novel pole figure inversion method: specification of the *MTEX* algorithm, J. Appl. Crystallogr. 41 (6) (2008) 1024–1037.

[45] S. Osher, R. Fedkiw, Level Set Methods and Dynamic Implicit Surfaces, Springer New York, NY, 2003.

[46] D. Cohen-Or, D. Levin, A. Solomovici, Contour blending using warp-guided distance field interpolation, in: Proceedings of Seventh Annual IEEE Visualization '96, 1996, pp. 165–172.

[47] D. Cohen-Or, A. Solomovic, D. Levin, Three-Dimensional Distance Field Metamorphosis, ACM Trans. Graph. 17 (2) (1998) 116–141.

[48] T.J. Massart, K. Ehab Moustafa Kamel, H. Hernandez, Chapter 11 - automated geometry extraction and discretization for cohesive zone-based modeling of irregular masonry, in: Bahman Ghiassi, Gabriele Milani (Eds.), Numerical Modeling of Masonry and Historical Structures, in: Woodhead Publishing Series in Civil and Structural Engineering, Woodhead Publishing, 2019, pp. 397–422.

[49] J.A. Sethian, Fast marching methods, SIAM Rev. 41 (2) (1999) 199–235.

[50] L.J.H.W. Bastiaansen, J. Wijnen, K. Ehab Moustafa Kamel, T.J. Massart, R.H.J. Peerlings, Meshing strategy for cohesive heterogeneous microstructures using distance fields and level sets, 2023, in preparation.

[51] W.G. Feather, H. Lim, M. Knezevic, A numerical study into element type and mesh resolution for crystal plasticity finite element modeling of explicit grain structures, Comput. Mech. 67 (2021) 33–55.

[52] P. Reu, All about speckles: speckle size measurement, Exp. Tech. 38 (6) (2014) 1–2.

[53] International Digital Image Correlation Society, in: E.M.C. Jones, M.A. Iadicola (Eds.), A Good Practices Guide for Digital Image Correlation, 2018.

[54] S. Shafqat, J.P.M. Hoefnagels, Cool, dry, nano-scale DIC patterning of delicate, heterogeneous, non-planar specimens by micro-mist nebulization, Exp. Mech. 61 (2021) 917–937.

[55] T. Vermeij, J.P.M. Hoefnagels, Plasticity, localization, and damage in ferritic-pearlitic steel studied by nanoscale digital image correlation, Scr. Mater. 208 (2021) 00.
[56] A. Orozco-Caballero, D. Lunt, J.D. Robson, J. Quinta da Fonseca, How magnesium accommodates local deformation incompatibility: A high-resolution digital image correlation study, Acta Mater. 133 (2017) 367–379.
[57] Z. Chen, S.H. Daly, Active slip system identification in polycrystalline metals by digital image correlation (DIC), Exp. Mech. 57 (1) (2016) 115–127.
[58] F. Bourdin, J.C. Stinville, M.P. Echlin, P.G. Callahan, W.C. Lenthe, C.J. Torbet, D. Texier, F. Bridier, J. Cormier, P. Villechaise, T.M. Pollock, V. Valle, Measurements of plastic localization by heaviside-digital image correlation, Acta Mater. 157 (2018) 307–325.
[59] A.P. Ruybalid, J.P.M. Hoefnagels, O. van der Sluis, M.P.F.H.L. van Maris, M.G.D. Geers, Mixed-mode cohesive zone parameters from integrated digital image correlation on micrographs only, Int. J. Solids Struct. 156 (2019) 179–193.
[60] J. Wijnen, J.P.M. Hoefnagels, M.G.D. Geers, R.H.J. Peerlings, Discrete slip simulations of ferrite microtensile tests: dislocation source stochastics, slip system activity and non-schmid effects, 2023, submitted for publication.
[61] C. Du, J.P.M. Hoefnagels, R. Vaes, M.G.D. Geers, Plasticity of lath martensite by sliding of substructure boundaries, Scr. Mater. 120 (2016) 37–40.
[62] S. Morito, X. Huang, T. Furuhara, T. Maki, N. Hansen, The morphology and crystallography of lath martensite in alloy steels, Acta Mater. 54 (19) (2006) 5323–5331.
[63] C. Du, R. Petrov, M.G.D. Geers, J.P.M. Hoefnagels, Lath martensite plasticity enabled by apparent sliding of substructure boundaries, Mater. Des. 172 (2019) 107646.
[64] F. Maresca, V.G. Kouznetsova, M.G.D. Geers, On the role of interlath retained austenite in the deformation of lath martensite, Modelling Simul. Mater. Sci. Eng. 22 (4) (2014) 045011.
[65] J. Inoue, A. Sadeghi, T. Koseki, Slip band formation at free surface of lath martensite in low carbon steel, Acta Mater. 165 (2019) 129–141.
[66] L. Morsdorf, O. Jeannin, D. Barbier, M. Mitsuhara, D. Raabe, C.C. Tasan, Multiple mechanisms of lath martensite plasticity, Acta Mater. 121 (2016) 202–214.
[67] L. Liu, F. Maresca, T. Vermeij, J.P.M. Hoefnagels, M.G.D. Geers, V.G. Kouznetsova, An integrated experimental-numerical study of martensite/ferrite interface damage initiation in dual-phase steels, Scr. Mater. 239 (2024) 115798.
[68] T. Nyyssönen, M. Isakov, P. Peura, V.T. Kuokkala, Iterative determination of the orientation relationship between austenite and martensite from a large amount of grain pair misorientations, Metall. Mater. Trans. A 47 (6) (2016) 2587–2590.
[69] R. Hielscher, T. Nyyssönen, F. Niessen, A.A. Gazder, The variant graph approach to improved parent grain reconstruction, Materialia 22 (2022) 101399.
[70] F. Niessen, T. Nyyssönen, A.A. Gazder, R. Hielscher, Parent grain reconstruction from partially or fully transformed microstructures in MTEX, J. Appl. Crystallogr. 55 (1) (2022).
[71] F. Maresca, V.G. Kouznetsova, M.G.D. Geers, Reduced crystal plasticity for materials with constrained slip activity, Mech. Mater. 92 (2016) 198–210.